TAMPEREEN TEKNILLINEN YLIOPISTO
TAMPERE UNIVERSITY OF TECHNOLOGY

ANTTI PALDANIUS

EVALUATION OF VIBRATION ASSESSMENT OF STERNOTOMY

Master of Science Thesis

Examiner: Professor Jari Hyttinen

ABSTRACT

ANTTI PALDANIUS: Evaluation of vibration assessment of sternotomy
Tampere University of Technology
Master of Science Thesis, 71 pages
September 2018
Master's Degree Programme in Electrical Engineering
Major: Biomedical instrumentation
Examiner: Professor Jari Hyttinen

Keywords: segmentation, ITK-SNAP, sternum, costal cartilage, ANSYS, MeshLab, Netfabb, finite element method, vibration measurement, harmonic response analysis, phantom

Median sternotomy is a common way to gain access to the heart during heart surgery. Early detection of sternal instability could prevent serious, potentially fatal, complications of sternotomy. Tays Heart Hospital has been developing a vibration measurement device for detection of sternal instability in cooperation with Tampere University of Technology. The device has been tested on sternotomy patients and cadavers but in both cases there are many variables such as geometry and material properties of the tissues of the individual test subject.

In this thesis cadaver measurements, phantoms and finite element method were used determine how material properties and the nature of the defect in the measured geometry affected the frequency response to the vibration sweep produced by the device. Phantoms were built from roughly tissue equivalent materials of known material properties and with simple geometry. Measurement results with the vibration measurement device were obtained from one cadaver and four phantoms.

Finite element models of the phantoms, cadaver thorax and simplified thorax geometries were created and simulated in ANSYS using Harmonic Response analysis. Unfortunately, the model created from the computed tomography data of the cadaver didn't work due to problems with geometry quality and meshing but results from the two other types of models were obtained. These results were then compared to measured data.

The measurement results from the phantoms indicate that the vibration measurement device requires some design changes to improve its accuracy and repeatability of the measurements. The finite element method simulation results indicate that depending on geometry and material properties the differences between a healthy sternum and a sternum with small defects may be hard to detect with vibration measurement but once the defect grows the frequency response changes significantly.

TIIVISTELMÄ

ANTTI PALDANIUS: Rintalastan värinämittauksen mallinnus
Tampereen teknillinen yliopisto
Diplomityö, 71 sivua
Syyskuu 2018
Sähkötekniikan diplomi-insinöörin tutkinto-ohjelma
Pääaine: Biolääketieteen instrumentointi
Tarkastaja: professori Jari Hyttinen

Avainsanat: segmentointi, ITK-SNAP, rintalasta, kylkirusto, ANSYS, MeshLab, Netfabb, elementtimenetelmä, värinämittaus, harmoninen vaste, fantomi

Sternotomiassa rintalasta halkaistaan, jotta kirurgi pääsee käsiksi sydämeen. Jos sternotomian jälkeiset ongelmat rintalastan paranemisessa havaittaisiin ajoissa, voitaisiin välttyä vakavilta, jopa kuolemaan johtavilta komplikaatioilta. Tays Sydänsairaala on kehittänyt värinämittauslaitetta rintalastan paranemiseen liittyvien ongelmien havaitsemiseen yhteistyössä Tampereen teknillisen yliopiston kanssa. Värinämittauslaitetta on testattu sternotomiapotilailla ja kadaavereilla, mutta kummassakin tapauksessa on paljon laitteesta riippumattomia muuttujia, kuten kudosten materiaaliominaisuudet ja geometria.

Tässä opinnäytetyössä käytettiin mittaustuloksia kadaavereista ja fantomeista ja elementtimenetelmällä tuotettuja simulaatiotuloksia värinämittauslaitteen toiminnan arviointiin. Työssä tutkittiin materiaaliominaisuuksien ja mittauksen kohteena olevan kappaleen defektien vaikutusta mittaustuloksiin. Fantomit rakennettiin materiaaliominaisuuksiltaan suurin piirtein kudoksia vastaavista materiaaleista. Fantomeiden geometria pidettiin yksinkertaisena. Mittaustuloksia saatiin yhdestä kadaaverista ja neljästä fantomista.

Mittauksissa käytetyistä kadaaverin rintakehästä ja neljästä fantomista tehtiin kolmiulotteisen mallit, jotka vietiin ANSYS elementtimenetelmäohjelmaan ja niiden värinävastetta simuloitiin. Lisäksi luotiin kaksi yksinkertaista rintakehän mallia, joiden värinävastetta simuloitiin. Valitettavasti kadaaverin rintakehän tietokonetomografiakuvista luotu malli ei tuottanut tuloksia geometrian laadun ja elementtiverkon ongelmien vuoksi. Fantomeidesta ja yksinkertaisista rintakehän malleista saatiin simuloitua värinävaste. Näitä tuloksia verrattiin mittaustuloksiin.

Fantomeiden mittaustuloksista havaittiin laitteen tarvitsevan joitain parannuksia, jotta sen tarkkuus ja mittausten toistettavuus paranisivat. Elementtimenetelmällä saaduista simulaatiotuloksista voidaan päätellä, että terveen rintalastan ja leikatun rintalastan ero on hyvin pieni, ellei rako leikatun rintalastan puoliskojen välillä kasva. Raon kasvattaminen muuttaa värinävastetta huomattavasti. Sekä mittaustulosten, että simulaatiotulosten perusteella voitiin tehdä joitain parannusehdotuksia laitteeseen.

PREFACE

This thesis was made as one part of the project on the vibration measurement device by Tays Heart Center and Tampere University of Technology. I previously completed my BSc for the same project and got an opportunity to complete my MSc for the same project. For this I am grateful to Professor Jari Laurikka and Juha Hautalahti, M.D, from Tays Heart Center and to Professor Jari Hyttinen from Tampere University of Technology.

The thesis topic was decided on and the research done in the thesis was planned in late 2016. The first measurements and cadaver computed tomography images were obtained in December 2016 and the practical work on the thesis begun. The year 2017 was spent on segmenting the tissues from the computed tomography images, learning to use finite element method and on creating the thorax finite element model. In early 2018 the phantoms and simpler thorax models were included because of the continuous technical issues with the segmentation based finite element model. This approach finally lead to results.

I'd like to thank everyone who has helped with this project and thesis. MSc Atte Joutsen was great help on the MATLAB analysis code, Professor Reijo Kouhia and MSc Shinya Abe introduced me to the world of finite element method, Irina Rinta-Kiikka helped me to better understand computed tomography imaging parameters and image segmentation and MSc Janne Koivisto helped me with measurement of material properties. Special thanks for Juha Hautalahti, M.D, for his feedback, ideas and instrumental part in practical measurements for the thesis and to Professor Jari Hyttinen for his guidance, feedback and ideas for the thesis.

Thanks to the SM401 break room crew for many great discussions. Finally, I'd like to thank my friends and especially my family for support during this thesis and rest of my studies.

Tampere, 13.09.2018

Antti Paldanius

TABLE OF CONTENTS

LIST OF FIGURES

LIST OF SYMBOLS AND ABBREVIATIONS

3D	Three dimensional
BMI	Body mass index
CAD	Computer-aided design
CT	Computed tomography
DSWI	Deep sternal wound infection
FEM	Finite element method
FFT	Fast Fourier transform
HU	Hounsfield unit
PLA	Polylactic acid
ROI	Region of interest
THUMS	Total Human Model for Safety
g	unit of acceleration; 1 g ≈ 9.81 m/s²

1. INTRODUCTION

Median sternotomy is a common way to gain access to heart for surgery. In this procedure the sternum is cut in half along the midline and usually closed with steel wires after the operation. Exact number of median sternotomies performed annually worldwide is unknown but it has been estimated to be over 2 million operations [1]. Serious complications such as mediastinitis are rare but potentially fatal [2]. These complications are often associated with sternal instability [3] and currently the diagnosis of sternal instability is mostly based on palpation by hand [4]. Imaging techniques such as computed tomography (CT) provide little information about healing of a sternotomy [5].

Hautalahti et al. [4] concluded that new tools are required for detecting early sternal separation and they have been developing a sternal vibration measurement device for evaluation of healing of a sternotomy. The device uses an actuator to produce a low frequency vibration sweep and an accelerometer to measure the response to the sweep. The actuator and the accelerometer are placed on opposing costal cartilages about 3 cm from the midline of the sternum. The accelerometer is measuring the vibration transmitted through the sternum and in theory the sternotomy, possible defects and complications and the healing process have an effect on the measured frequency response of the sternum. N. Beev developed the first two versions of the vibration measurement device and the preliminary study produced some promising results indicating that healing of the sternotomy had an effect on the frequency response [4, 6].

The vibration measurement device has been tested on patients in a preliminary study and on cadavers in a yet unpublished study. The purpose of this thesis is evaluating the function of the vibration measurement device through measurements and simulation in a more controlled and repeatable way. As the geometries used in this thesis are complex it is not possible to obtain analytical mathematical solutions for them. Finite element method (FEM) offers a solution to this problem. In FEM a continuous domain, for which obtaining an analytical solution is impossible, is discretized into finite number of elements. Equations are formulated for each element and are combined to obtain a solution for the entire domain. [7]

There were no previous literature examples of finite element models of thorax where low frequency vibration was simulated. However multiple examples of other mechanical finite element models of thorax were available [8-15]. The models were either simulating impact forces on the rib cage [9, 10, 12, 14, 15] or the deformation of the rib cage during breathing [8, 11, 13]. One example of finite element modelling of vibrational behavior of femur was found in literature [16].

The aim of this thesis is to provide more controlled testing method for the vibration measurement device and to use simulation to predict what kind of vibration response can be expected with different kind of post-sternotomy defects in the sternum. As the effect of the material properties of the measured body to the results provided by the device have not been previously explored this thesis also aims to do that with FEM simulation.

When using humans as test subjects the problem is the variable geometry and material properties between individuals, so measurement results between individuals are not comparable. Even changes in the same living individual, for example weight gain, are expected to change the results. In addition, it is not possible to induce defects on a living person to see what kind of effect they have on the frequency response of the sternum. This leads to need to build phantoms from tissue equivalent materials for evaluation of the device as the geometry can be easily controlled and material properties are known.

As the phantoms will have less materials and simpler geometry than a real human subject, simulation of more complex geometries can be used to complement the measurement results. Three dimensional (3D) models created from segmented CT data has been used in FEM simulations in previous research [11, 13, 17] so this approach will be explored in this thesis in addition to simulation of the phantoms and simpler models. Measurement results from the phantoms and a cadaver will be used to establish a baseline for the simulations.

2. BACKGROUND

2.1 Anatomy of thorax

The bones of the thorax form the thoracic cage. It consists of the sternum, ribs and thoracic vertebrae. The sternum is anterior to the heart and consists of three pieces: manubrium, body and xiphoid process. It forms an enclosure for the lungs and the heart and provides attachment for upper limb and pectoral girdle. [18]

The manubrium is the uppermost portion of the sternum. The manubrium connects to the clavicles with ligaments and there is an articular disk between each clavicle to and the clavicular notches of the manubrium. [19] The manubrium connects to the first ribs with costal cartilage. The manubriosternal joint connects the manubrium to the body of the sternum at the sternal angle. The second rib attaches at the level of manubriosternal joint. The body of the sternum is the longest part and ribs 3 to 7 attach to it. Xiphoid process is at the inferior end of the sternum and it provides an attachment point to some abdominal muscles. [18]

There are 12 pairs of ribs all of which are connected to the vertebral column at their posterior end. Ribs 1 to 7 are connected to the sternum from their anterior end with a strip of hyaline cartilage called the costal cartilage. Ribs 8, 9 and 10 attach to costal cartilage of rib 7 and ribs 11 and 12 don't attach to anything at their anterior end but are embedded in surrounding muscle. Ribs 1 to 7 are called true ribs and 8 to 12 are called false ribs. [18]

Between the ribs are 11 pairs of external intercostal muscles which lie superficially between the ribs and 11 pairs of internal intercostal muscles which lie behind the external muscles between the ribs. Diaphragm is located between the abdominal and thoracic cavities and it has openings for esophagus and major blood vessels. Diaphragm and external intercostal muscles are responsible for inhalation in respiration and internal intercostal muscles are used in forced expiration to empty the lungs as fast as possible. [18]

Inside the thoracic cage is the thoracic cavity which contains the heart and the lungs. The heart is located in the mediastinum between the lungs and behind the sternum. Lungs are surrounded by the pleura and the heart is surrounded by the pericardium. [18]

The thoracic cage is covered by muscles such as pectoralis major, pectoralis minor and external oblique muscle. There is a layer of varying thickness of adipose tissue on top of the muscles and skin over the adipose tissue. [19]

2.2 Median sternotomy

2.2.1 Surgical procedure and complications

Median sternotomy is commonly performed surgery which provides access to the mediastinum and hilar structures of the lungs. It was introduced in 1897 and was initially known as “Milton’s procedure” but it was not used much until the cardiac surgery field blossomed in 1950s [20].

In median sternotomy the patient is placed supine and one or both hands placed at the side. Neck is extended by placing a roll behind the shoulders. This exposes the sternal notch. The midline of the sternum is marked, the skin and the subcutaneous layers are divided and the midline of the exposed sternum is marked with cautery. The midline is identified by palpating the intercostal spaces. Both the interclavicular ligament and xiphoid tip are divided and the space posterior to them is bluntly dissected. The sternum is then divided with a reciprocating saw. Bleeding is cauterized and sternal retractor is used to spread the sternal halves apart. When the operation is completed chest tubes are inserted, the sternum is closed with steel wires and the tissues on top of it are sutured close. [21]

Some serious complications like deep sternal wound infection (DSWI) and mediastinitis are associated with median sternotomy [20]. Such failure to heal is a rare complication [2]. Both DSWI and mediastinitis can be fatal and even when treated correlate with higher mortality in the long term [20].

In a review of 73,700 cases by Kubota, Miyata et al. [22] the overall incidence of DSWI after a sternotomy operation was 1.8%. The overall mortality of DSWI patients was 9.7% and the operative mortality was 25.8%. According to Atkins Zane and Wolfe Walter [20] sternal instability is one of the mechanisms contributing to development of sternal infection.

According to Aykut, Albayrak et al. [23] early repair of sternal instability prevents mediastinitis. In their study of 1440 patients 85 or 5.9% developed post-sternotomy sternal dehiscence but only two progressed to mediastinitis as the sternal instability was quickly treated.

2.2.2 Clinical assessment of healing of sternotomy

Currently the diagnosis of sternal instability is still largely based on palpation [4]. The physical examination consists of firm, bimanual palpations of the sternal halves [24]. Signs like sternal click, pain and movement during the palpations or sternal movement

when coughing or breathing are indicative of sternal dehiscence and instability [24, 25]. There is no standardized way of performing the physical examination. El-Ansary, Adams et al. [26] suggested a rating scale for quantifying sternal instability in patients but there aren't any mentions of its adoption by others in literature.

Boiselle, Mansilla et al. [25] studied the presence of sternal wire abnormalities in post-operative chest radiographs of 19 patients with diagnosed sternal dehiscence. It was determined that 17 of the patients had visible sternal wire abnormalities in their chest radiographs with 13 of them having abnormalities present 1 – 6 days prior to the diagnosis of sternal dehiscence. While 70 % of the patients diagnosed with sternal dehiscence showed signs of sternal wire abnormalities in their chest radiography only in 20 % of the cases the radiography results had direct or indirect impact on the diagnosis. In the control group of 19 patients no sternal wire abnormalities were observed in the post-operative chest radiographs. Boiselle, Mansilla et al. concluded that there is more potential in chest radiography as a tool to help detection of sternal dehiscence.

In their follow up study Boiselle, Mansilla et al. [27] included patients with diagnosed sternal dehiscence with and without mediastinitis. In both groups it was observed that sternal wire abnormalities were present in majority of the patients. They concluded radiography could be useful in detection or diagnosis of these complications.

According to Bitkover, Cederlund et al. [5] computed tomography was used in Karolinska Hospital, Sweden, as a diagnostic tool for complications of median sternotomy. They didn't know its efficiency, so they ran two studies on two groups of patients. The first group had 20 patients with normally healing sternotomy with CT scans taken at 1 week, 1 month, 3 months and 6 months after the median sternotomy. The second group was 65 patients with suspected postoperative complications. 87 CT scans were performed on this group.

In the first group studied none of the CT scans showed signs of healing at 3 months and at 6 months only half of the patients had fully healed sternum. Gaps up to 3 mm did not correlate with clinical instability and gaps seen in CT didn't always indicate sternal dehiscence. On the second group 38 scans were performed because of sternal pain or suspected dehiscence and 49 scans because of suspected infection. Only 11 of the 38 scans resulted in diagnosis of dehiscence or pseudarthrosis and only seven scans of the 49 showed signs of mediastinitis with two being false positives and mediastinitis being actually present in 16 of the scans. Bitkover, Cederlund et al. [5] concluded that there is no correlation with computed tomography images and clinical healing of the sternotomy and that CT is not sensitive tool for diagnosing mediastinitis and it adds very little information in patients with sternal pain. Their state the only sure way to diagnose mediastinitis is a positive culture from mediastinal fluids or tissues.

In CT images most patients have gaps up to 4 mm wide, overriding of the sternal halves or sternal halves at different levels [28]. According to Li and Fisherman CT can be helpful in detection of complications such as dehiscence, paramedian sternotomy, mediastinitis and osteomyelitis. CT findings indicating dehiscence include sternal wire abnormalities and widening of the gap between the sternal halves but detecting these changes requires multiple post-operative CT scans thus increasing the radiation dose to the patient and cost to the health care facility.

Use of ultrasound as a tool for quantification of sternal instability was studied by El-Ansary, Waddington et al. [29]. In their method the ultrasound head was suspended on the patient's chest with an extensible stand. The maximum separation of the sternal halves was measured during rest and five different upper body movements. They concluded that ultrasound measurement of sternal separation had high reliability. All the patients in the study had pre-diagnosed gross sternal instability so the ultrasound didn't provide any aid in diagnosis of sternal dehiscence.

These studies indicate that imaging methods like CT, radiography and ultrasound have little diagnostic value in early detection of sternal dehiscence. Defects are common in normally healing sternotomy incisions and do not indicate sternal instability [5, 28]. Secondary findings like shifting of sternal wires may provide some aid in diagnosis of sternal dehiscence [25, 27] but even three months after the surgery there were no radiological signs of healing of the sternum [5]. Manual palpation remains the primary method of evaluation of post-operative sternal stability [4].

2.3 Vibration measurement techniques

2.3.1 Vibration transmission and damping

Vibration is a pressure wave transmitted through a solid object. It's similar to sound which is air or water bourn acoustic vibration [30]. How well vibration transmits through a structure is determined by mass, stiffness and damping of the structure. While mass and stiffness are generally known material properties damping is unpredictable and complex property. Damping is present in every dynamic system and its form of mechanical energy dissipation. There are many physical mechanisms involved in damping; viscosity, friction, temperature, shape, acoustic radiation, turbulence and mechanical and magnetic hysteresis. Loss factor, damping ratio and percent of critical damping are dimensionless numbers which are used to express effectiveness of vibration damping in a structure. In viscoelastic materials the energy loss of the vibration is caused by heat generated by cyclic deformation of the material. [31]

When doing vibration analysis damping is generally represented by simplified models as it's not practical to implement microscopic representations of damping such as grain

boundaries and impurities in internal damping of the material. In vibration analysis hysteric and viscoelastic damping are the two forms of internal damping. Structural damping represents mechanical energy dissipation due to friction between components and by intermittent contact or impacting at the joins of the structure. Fluid damping represents fluid-structure interactions. The former two are of interest in this thesis. [32]

In human body the soft tissues act as damping material and natural frequencies for muscles like the triceps surae, quadriceps and tibialis anterior have been measured to be from ~10 Hz in relaxed state and up to 50 Hz in fully active state. This provides damping for example against vibrations caused by heel strike during walking or running. [33]

Bones have been measured to have higher resonant frequencies than soft tissues. For example, the resonant frequency of human tibia ranges between 300 and 500 Hz. Tsuchikane et al. measured natural frequency of human tibia from five cadaveric legs. In order to evaluate the effects of soft tissues they conducted measurements from intact legs and then removed skin, muscles and joints of the tibia. They concluded that removing soft tissues such as muscles reduced the damping ratio and caused substantial increase in the resonant frequency. On average the damping ratio of the intact leg was 0.19 while the damping ratio of the tibia alone was just 0.03. [34]

2.3.2 Vibration measurement of bone

Vibration analysis has been proposed as a non-invasive technique for analysis of mechanical properties of healing bones [35]. However the development of such techniques has been slow because the relationships between fracture callus strength, bone geometry and measurement conditions are not well understood [36].

Rowlands et al. used low frequency (< 1500 Hz) vibration and Sawbones® femur and a phantom build from Tufnol® tubing immersed in a water bath to determine if vibration analysis could be used as a way to detect hip prosthesis loosening in-vivo. They measured the vibration response with both an ultrasound probe and an accelerometer. According to their results vibration measurement has potential to be a non-invasive method for detection of prosthesis loosening in vivo. [37]

According to Nokes et al. when measuring induced vibrations on bone with skin mounted accelerometers preloading is important because of the damping effect of the soft tissues. However, with sufficient preloading the skin mounted accelerometer provided similar results to an accelerometer directly mounted to the bone. The required amount of preloading varied a bit depending on the thickness of the soft tissue layer on top of the bone and excessive preloading distorts the recoded signal with a high frequency component. They concluded that for skin thickness of 2 mm preloading of 3.8-5.2 N produces good results. [38]

A vibration measurement device for early detection of post-operative sternal instability has been under development since 2010 by Juha Hautalahti et al. as there currently isn't a reliable way for early detection of sternotomy separation. According to their research vibration is used in experimental mechanical analysis of machine parts and structures. Experimental studies show change in resonant frequencies of broken bones and vibration has been used to assess bone density and implant stability. [4]

2.3.3 The sternal vibration measurement device

In the preliminary study that also inspired this thesis Hautalahti et al. tested a vibration measurement device with a frequency sweep of 50 to 1500 Hz and frequency response was measured with an accelerometer. 22 patients took part in the study but complete datasets were obtained from only 14 of them. According to their results there was significant decrease in vibration transmission post-operatively when compared to pre-operative control measurement. The vibration transmittance then increased as the healing of the sternum progressed. [4]

The idea of the device is comparing pre-operative vibration transmittance results to the post-operative results. The pre-operative results act as a baseline and the healing process can be followed with post-operative measurements. If the vibration transmission of the sternum starts to decrease during the post-operative period, it would indicate sternal separation. Cadaveric measurements have shown a significant decrease in total power (g^2/Hz) between pre-operative, normal post-operative and sternal separation conditions.

The vibration measurement device has an actuator and an accelerometer. The actuator is placed on the skin on top of a costal cartilage and it's used to produce an excitation which in this case is a sinusoidal vibration sweep while the accelerometer is placed on the opposite side of the sternum on the skin on top of a costal cartilage. Both the actuator and the accelerometer are held by hand. The accelerometer measures the vibration coming through the sternum to the costal cartilage on the opposite side of the actuator and in theory defects in the sternum have an effect on the transmission of vibration through it. Both the actuator and the accelerometer are preloaded to reduce the damping effect of soft tissues.

The first iteration of the vibration measurement device had the sensor and actuator directly connected to a laptop but it has been since developed into a battery operated standalone device which saves the measured data on a USB memory stick. These variants were developed by Nikolai Beev [6]. A more streamlined unit was built by Esa Jaatinen and this version is undergoing testing with cadavers. This version has parts touching the body made out of Teflon and can be sterilized with autoclave.

The current version of the vibration measurement device has an actuator which produces a vibration sweep from 20 Hz to 2000 Hz. The actuator is build out of Series 65 latching

solenoid which axis has been replaced with a magnet. The waveform of the current through the solenoid is square wave which is pulse width modulated to produce the vibration sweep. The part that touches the patient is made out of Teflon and has embedded piece threaded rod to which the magnet attaches. For measuring the frequency response, it uses a LIS352AR low power 3-axis accelerometer which has ±2 g scale and maximum bandwidth of 2 kHz. The signal from the Z-axis of the accelerometer is recorded at 10 kHz sample rate and saved on an external USB memory. Both the actuator and the accelerometer are preloaded by springs. The data used in this thesis has been measured with this version of the device.

2.4 FEM and mechanical modeling

2.4.1 Finite element method

The concept of simplifying a continuum problem by representing it as finite elements was introduced in 1956 by Turner, Clough, Martin and Topp [39]. In these early models a two-dimensional domain was represented with triangular panels which had elementary stiffness matrices to represent their behavior under load. Rapid development of the finite element method begun in 1960s and by the end of the decade many books were published about the finite element method.

In the finite element method, a continuous domain, in this case a geometric region is divided into geometrically simple subdomains called finite elements. Governing functions of the problem are solved for each individual element and the complete solution for the domain is generated by assembling the solutions of the individual elements. [40, 41]

The solution is not exact but an approximation as the domain assembled from the individual finite elements may not be exactly the same size and shape as the original domain. Another stage where errors can be introduced when element equations are derived. Generally unknown dependents in a continuous function over the domain are represented by a linear combination of known functions and undetermined coefficients. This can introduce approximation errors into the solution. Errors can be introduced in the final solving phase of the assembling the system of equations. If all the above errors are zero an exact solution is found but that is usually not the case. [41]

Division of the domain into discrete elements is called meshing. 3-dimensional geometry such as that used in this thesis can be meshed into a tetrahedral mesh, a quadric mesh or a combination of the two.

Setting up FEM simulation generally requires boundary conditions for the domain or domains simulated. There are multiple different kind of boundary conditions that can be applied depending on the simulation type. In mechanical simulation boundary conditions either constrain or act up the model by either fixing it in such way it can’t deform or by

exerting forces on it. In this thesis boundary conditions used are fixed supports, loads and contacts between different domains.

When solving a problem with FEM it's important to select a suitable mathematical model for the problem as the solution will not produce any information not contained in the model. The mathematical model which produces results within an acceptable error while using least amount of computational resources is the most effective. The accuracy of the results can be improved by refining the finite element mesh, solution parameters, presentation of loading and boundary conditions etc. If the results are still inaccurate the mathematical model has to be improved or changed to better suit the problem in question. [42]

Today FEM is used to solve variety of engineering problems involving stress analysis, electromagnetism, heat transfer and fluid flow [40]. On the field of biomedical engineering FEM is used mostly in research applications such as simulating femur fractures [43, 44], development of custom patient specific knee joint prosthesis [45], analysis of proximal femur strength [17], analysis of blood flow and stresses in abdominal aorta [46-48] etc. There are countless of studies about finite element models of different electrical, mechanical and fluid flow phenomena in the human body.

2.4.2 FEM models of the mechanics of the human thorax

Previous research on FEM models of human thorax are from variety of different fields. Some examples include chest wall model to predict tumor movement during respiratory cycles [8], side impact analysis to predict thoracic injuries during car accidents [9], model of human rib cage to recognize stress distributions and rate of bone fractures [10], using FEM analysis to plan treatment for funnel chest deformation [11], model of behavior of costal cartilage during car accidents [12] and biomechanical simulation of thorax deformation during respiration [13].

In literature there were two main approaches to building FEM models of the human thorax. Some of the models were based on patient data [8, 11, 13] while others were made with computer-aided design (CAD) software based on anatomical drawings, commercial data packages or other measurements [9, 10, 14] and one model was obtained from external source, Total Human Model for Safety (THUMS) from Toyota [12]. Making a model from patient data requires a volumetric image of the patient such as a CT image. The tissue types needed for the model were segmented from the CT image and converted into a format from which a finite element mesh could be generated. In one case it was found to be too difficult to segment intercostal muscles and the diaphragm so they were recreated from anatomy book images and added to the model [13]. See Table 1 for comparison of different approaches taken in literature to building finite element models of thorax.

Table 1. Comparison of FEM models of thorax in literature

Author	Origin of geometry data	FEM software	Tissue types	Number of elements
Didier, Villard et al.	CT image	Code-Aster	Skin, lungs, bone	130,000
Furuse, Watanabe et al.	Commercial data packages and anatomy books	PAM-CRASH	Cortical bone, cancellous bone, costal cartilage, diaphragm, intercostal muscles, internal organs as homogenous viscus	83,500
Awrejcewicz and Luczak	Anatomy book	ANSYS	Bone, cartilage	N/A
Gzik-Zroska, Wolański et al.	CT image	ANSYS	Bone, cartilage, intervertebral discs	11,434
Oyen, Murakami et al.	Toyota THUMS	N/A	Costal cartilage, cortical and cancellous bone	N/A
Zhang, Chen et al.	CT image and anatomy book	ANSYS	Bone, cartilage, intercostal muscles, diaphragm	252,795

Didier, Villard et al. [8] built a chest wall model including the skin, the ribs, the pleura and the soft tissue between the skin and the ribcage. They used FEM to compute motions and deformations of the model during breathing cycles. The geometry for their model was obtained by segmenting lungs, skin and rib cage from two CT image sets; one at the end of exhalation and one at end of inhalation. They created a tetrahedron mesh of 21000 vertices and 130000 elements and used inverse kinematics in Code-Aster software to build a model which allows to correlate the thoracic outer surface and lung motion. They plan to continue the research in future with more accurate model including the diaphragm, proper lung boundary conditions and the actual tumor.

Furusu, Watanabe et al. [9] published a paper on building a finite element model of the human thorax for impact analysis in car crashes. They built a model which includes the sternum, the ribs, the costal cartilages and the spinal column. Internal organs inside the

thorax were modeled as homogenous viscus. They used the model for side impact analysis and compared the results to cadaver data. According to their conclusion their thorax finite element model produced similar results to human cadavers in side impact test and that their thorax model is good enough to calculate injury data from. This model was used as a part of the THUMS model from Toyota [14].

Jan Awrejcewicz and Bartosz Luczak [10] built a model of the rib cage based on anatomical drawings and measurements found in atlases of human anatomy. They simplified the model by neglecting costochondral, intercostal and interchondral joints, simplifying the complex curves of the ribs and by using a homogeneous, isotropic and linear material to approximate the heterogeneous, anisotropic and non-linear material properties of bones and cartilage. ANSYS was used to simulate a frontal impact on the sternum and the model was verified by comparing the results to cadaver data from similar tests. Another model was built to simulate effect of Nuss' implant which is used to repair pectus excavatum. The model predicted that in case of a car crash the implant would transfer force to the 5^{th} rib and cause earlier fracture with smaller force and the implant itself may damage the heart or the lungs.

Gzik-Zroska, Wolański et al. [11] used a finite element model to plan optimal treatment strategy for a patient with pectus excavatum. Pectus excavatum or the funnel chest is treated with Nuss procedure where a steel plate is inserted under the deformed sternum and used to correct the deformity. Their model was used to determine the optimal parameters for the steel plate. Mimic Materialise was used to generate the 3D geometry of the ribs, the sternum, the costal cartilages and the spinal column from the CT data of the patient. Mimics 3-matic was used to create and optimize a model composed of tetrahedral elements which was then exported to ANSYS. The model was simplified by considering the bones and cartilage as homogeneous bodies with isotropic properties and pressure inside the chest and the influence of internal organs was neglected. The stress and strain on the chest after the corrective surgery were simulated in ANSYS and optimum parameters for the corrective plate were simulated. The authors determined that this kind of virtual models could be used to prevent complications during the surgery.

According to research by Oyen, Murakami et al. [12] almost no mechanical examination has been performed on costal cartilage of the rib cage. They studied the mechanical stiffening of costal cartilage with age and its effect on injuries of elderly people in car accidents. They performed mechanical measurements on young porcine costal cartilage and on tissue from adult human cadavers to obtain data for the finite element model. The actual model was an individual rib "hoop" consisting of rib bones, the sternum, the vertebral body, costovertebral joint ligaments and the costal cartilage. It was based on measurements of 50^{th} percentile American male at 5^{th} rib level. They simulated steering wheel hub impact on the sternum and the loads caused by it to the rib cage with both soft and stiff costal cartilage. They found that the stiffening of the costal cartilage with age not only affected the deformation pattern but also the injury pattern.

Zhang, Chen et al. [13] simulated the deformation of the thorax during respiratory cycle with model of the rib cage, intercostal muscles and diaphragm. The bones and cartilage of the model were segmented from CT data of a patient, but they found out segmenting the muscles to be difficult from the CT image set so they referenced anatomy books when adding the muscles into the model by hand. They modeled the direction of the muscle fibers and simulated the resulting thorax deformation during muscle contraction. The model was validated by comparing the deformation results to 4D-CT images. Some deviation between simulation and clinical observations occurred in the rib and diaphragm movements and that was attributed to lack of cervical accessory muscles and viscosity effect of the airflow in the lung.

Previous research of finite element models of human thorax is mostly about behavior of the rib cage during an impact or simulating the respiratory movements and the resulting deformations. There was also a case where FEM was used to optimize treatment for pectus excavatum. According to the authors in all cases the models worked well and results were often comparable to real life tests and measurements even with simplifications like modeling the tissues as homogeneous and isotropic or modeling all organs inside the thorax as homogeneous mass.

2.4.3 Modeling vibration in ANSYS

The FEM software used in this thesis is ANYS 18.2. ANSYS is extensively used as a design tool and is available to students in many universities around the world. ANSYS can be used to solve multiple different kind of vibration problems; transient, natural frequency, harmonic response, response spectrum and random vibration. [49]

Vibration can be modeled in transient structural analysis as a load that is a function of time. For example, it can be included as sinusoidal force function or imported in table format (force as function of time) from MATLAB or actual measured data. Nonlinear effects like friction, plasticity and large deformations are allowed in transient analysis but including them can increase the solution time significantly. Young's modulus and density must be defined for each material in the model. When simulating vibration damping effects are important and in transient analysis damping controls allow inclusion of numerical damping, stiffness coefficient (Beta damping) and mass coefficient (Alpha damping).

Modal analysis can be used to determine the natural frequencies and mode shapes of the simulated model. The results from modal analysis can be used as a starting point for mode-superposition method in harmonic response, transient structural and spectrum analysis. The mode-superposition method saves computational time when compared to full method which uses full stiffness and mass matrices [49]. Nonlinearities are ignored in modal analysis and required material properties are stiffness in some form and density of the material. For damped systems stiffness coefficient can either be entered manually or

as function of frequency and damping ratio and mass coefficient is always entered manually.

In harmonic response analysis the system is assumed to be linear and loads vary sinusoidally with time. It is used to verify if a design can handle fatigue, resonance and other harmful effects of forced vibrations. Harmonic analysis does not calculate transient vibrations which occur at the beginning of the excitation and usually harmonic analysis is used to calculate response of the modeled structure to cyclic loads over a frequency range and to obtain a graph of frequency response of some quantity such as acceleration or displacement. As harmonic response is a linear analysis or nonlinear effects like friction and plasticity are ignored even if defined in the model. The harmonic analysis can be solved with either mode-superposition or full methods. In the former method results from modal analysis is used to perform linear combinations of eigensolutions. The full method is a direct integration method which uses the full system matrices for calculating a solution. It is more accurate than mode-superposition but requires more processing power and time. Harmonic response requires some form of stiffness and density as material property for each of the materials in the model. Constant damping ratio, stiffness coefficient and mass coefficient are available as system damping controls.

Response spectrum analysis is used in civil structure designs such as calculating wind loads for high-rise buildings or behavior of nuclear power plant designs under seismic loads. The responses it produces are deterministic maxima as in this type of analysis the maximum response is calculated based the input and modal responses. As it requires the modal responses a modal analysis is a prerequisite for it.

Random vibration analysis enables determination of response of structures to random vibration loads. A frequency spectrum of real-world random vibration such as car driving on pavement can be recorded and used as a load in this type of analysis. As this type of analysis uses mode-superposition method a modal analysis is prerequisite for it. Typical applications for random vibration analysis include electronic packaging and aerospace components which are subject to turbulence, engine vibration and acoustic pressures, analysis of response of structures to earthquakes, ocean wave loading on offshore structures and wind loads on tall buildings.

In this thesis the vibration analysis option of interest is the harmonic response analysis. The vibration measurement device produces a vibration sweep from 20 Hz to 2000 Hz and it can be simulated as a sinusoidal load in harmonic response analysis. The excitation produced by the vibration measurement device is small and doesn’t produce significant deformations in the measured system, so it should be safe to assume it can be simulated as a linear system.

3. MATERIALS AND METHODS

3.1 Phantom measurements

A simple phantom was built for testing the vibration measurement device. Clear Ballistics synthetic gel was used as a soft tissue analogue and rods made from 3D printed polylactic acid (PLA) were embedded in the gelatin to simulate stiffer and denser structures such as bone and cartilage. A defect was simulated by embedding a cut rod in the gel.

The goal of the measurements was to determine if the vibration measurement device produced repeatable results when multiple measurements were performed on the same phantom and to determine if different kind of defects and composition of the rod embedded in the gel had an effect on the results. Effect of increased thickness of the soft tissue analogue on top of the embedded rod on the frequency response was also tested. Measurements were also performed on the effect of external load being applied on the actuator.

3.1.1 Building the phantom

The size of the rods embedded in the synthetic ballistic gel was 20cm*2cm*1cm. The size was chosen to roughly represent a human rib. The PLA rods were made by 3D printing at 100% infill setting with Ultimaker 3D printer. One of the PLA rods was cut in half to simulate a defect, one was cut in half and then sutured back together with sternal closure steel wires and one was left intact. One gel block didn't have an embedded rod.

Clear Ballistics synthetic gel is reusable by melting the used gel in an oven and casting it in a mold. This property of the material was used in building the phantom as the synthetic gel could be melted in regular kitchen at temperature of 120 ºC. The gel was delivered as a block measuring 40 cm by 15 cm by 15 cm. The block was cut up in smaller pieces and the pieces were placed in a regular kitchen pot which was then placed in the warm oven.

Once the gel had melted it was left in the oven for some time to let air bubbles escape to ensure as homogeneous as possible constitution. After no air bubbles were present in the liquid gel the pot was removed from the oven and the gel was cast in a plastic container measuring 21 cm by 14 cm to 5cm height. Once the gel solidified the PLA rods were placed in the container on top of the gel and then another 12 mm high layer was cast in the container to provide approximately 2 mm layer of gel on top of the PLA rods. The gel blocks with now embedded PLA rods were left to cool down in the containers that also acted as molds for the casting process.

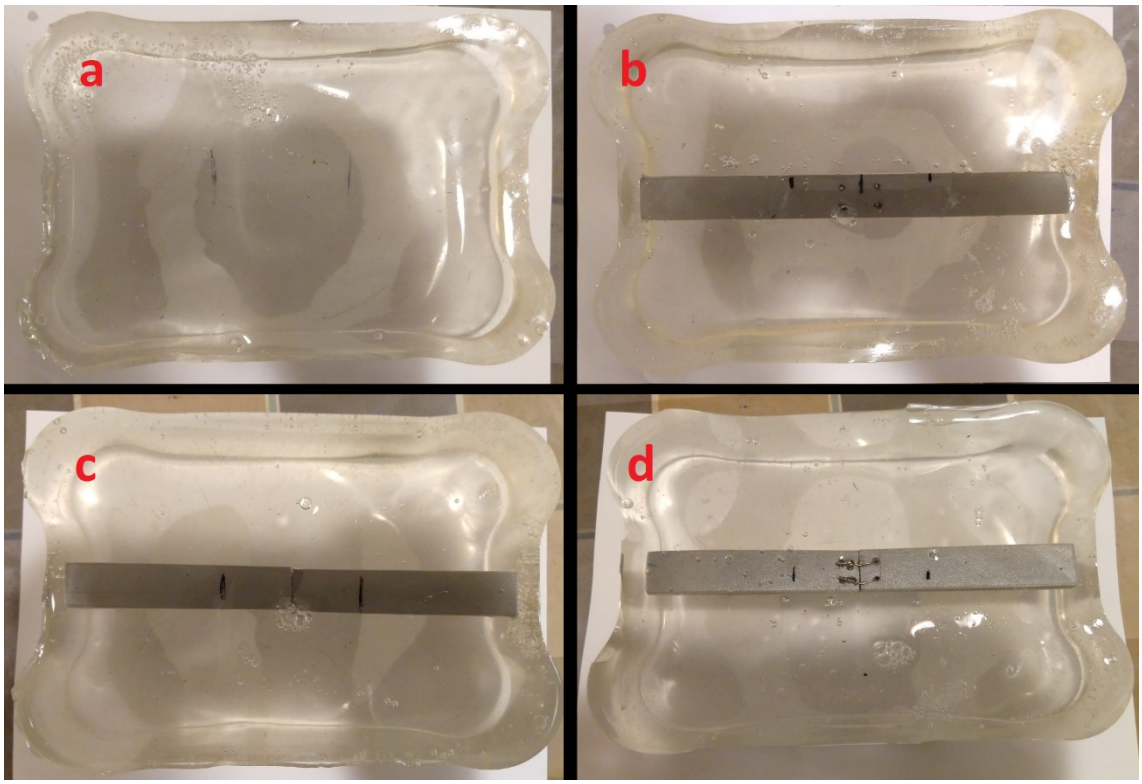

Figure 1. Phantoms built for testing the vibration measurement device. (a) is the gel block with no PLA rod, (b) has intact PLA rod, (c) has cut PLA rod and (d) has sutured PLA rod.

3.1.2 Material properties

The PLA rods were printed from silver grey PLA filament bought from Ultimaker's store. Mikael Virta [50] used the same Ultimaker 3D printer and same filament in his master's thesis and measured the Young's modulus of pieces printed by it to be between 1220 MPa and 1400 MPa. The larger 0.4 mm nozzle used to print the pieces used in this thesis produced parts with Young's modulus closer to the higher end of that spectrum. The nominal density of the PLA filament was 1.25 g / cm^3. According to Torres, Cotelo et al. [51] the Poisson's ratio for bulk PLA is 0.36.

As the material properties for the Clear Ballistics synthetic 10% ballistic gelatin equivalent were not known the properties needed to run ANSYS simulations were measured or obtained from available literature. Samples were prepared by melting the ballistic gel and casting it to a cylindrical mold with diameter of 12.2 mm. Once the gel solidified it was extracted from the mold and cut into shorter segments suitable for compression testing. Stress – strain charts were measured with BOSE Electroforce Biodynamics 5100 machine. The machine was set to compress the samples until 75% strain at 0.167 mm/s speed. It had to be calibrated each time for individual samples as the height of the samples varied a bit. None of the samples fractured or slipped during the measurement but a few

were slightly canted. A computer with Wintest 4.1 software was used to record the displacement and the force applied to achieve that displacement for each of the samples. This measurement setup for the machine was used by Koivisto et al. [52] for measurement of material properties of hydrogels.

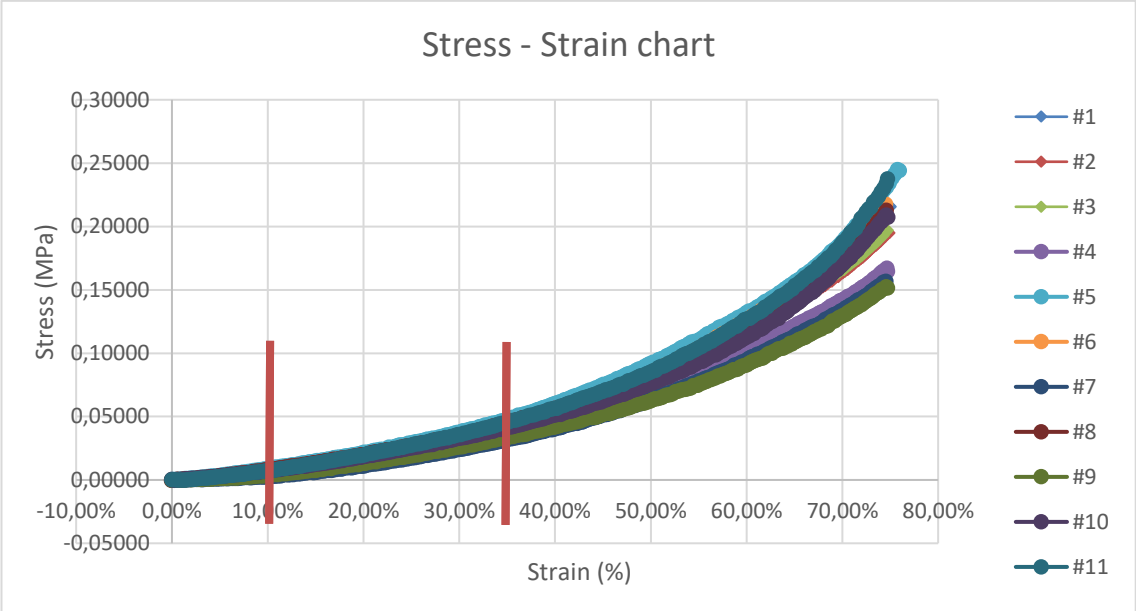

Figure 2. Stress - strain chart of all 11 measured samples. The vertical bars indicate the linear region from which compression modulus was calculated. The Excel data analysis sheet and plotting tool was modified from sheet originally made by Janne Koivisto and Hanna Kemppi with their permission.

The stress – strain data was then imported to Microsoft Excel 2016 where the data was plotted and the linear region of the stress – strain curves was visually determined to be between 10 % and 35 % strain. Data between those strain percentages was plotted and a trend line was fitted for each sample and a gradient was obtained. This gradient is the compressive Young's modulus of the material. The compressive Young's modulus varied between 116.9 kPa and 154.8 kPa depending on the sample with the median value being 139.3 kPa.

Table 2. Material properties for the materials used in the phantom

Material	**Density (g/cm³)**	**Poisson's ratio**	**Young's modulus (MPa)**
PLA	1.25	0.36	1220 - 1400
Clear Ballistics 10%	0.865	0.46	0.1393

Poisson's ratio for the ballistic gel was not measured due to lack of suitable equipment but it was assumed to be similar to Clear Ballistics synthetic 20% ballistic gelatin equivalent which was measured by Pasumarthy et al. [53] to be 0.46.

The density of the Clear Ballistics gelatin was calculated from volume and weight values provided by the manufacturer on their website [54].

3.1.3 Measurement setup for the phantoms

The phantoms were measured with the third version of the vibration measurement device. The phantoms were placed on a table. The distance between the actuator and the accelerometer was 6 cm in every measurement. For each phantom the midline was determined and the actuator was placed 3 cm left of the midline and the accelerometer was placed 3 cm right of the midline. The actuator and the accelerometer module were held by hand.

A series of ten measurements were performed on a phantom at a time and then the data was then transferred to a laptop and checked in MATLAB if it looked good as the device would sometimes just record static in the result files. Each phantom had at least two sets of ten measurements performed on it as it was noted that the results were affected by how much pressure was applied on the actuator and accelerometer so having large sets of data was necessary to average out measurement error.

3.1.4 Finite element model for the phantom

The dimensions of the phantoms were measured and the data was used to replicate the geometry in ANSYS SpaceClaim CAD software. The two-dimensional footprint of the phantom was first drawn on the x-y-plane and Pull-tool was used to extrude the footprint to 5 cm height which was the height the ballistic gel was cast in the molds before inserting the PLA rods. The footprint of the PLA rod was drawn on the plane on top of the gel block and it was extruded to 1 cm height to produce the geometry presenting it. The top of the gel block was then further extruded by 1.2 cm to cover the entire PLA rod with 2 mm gel layer as in the real-life phantom. The geometry of the PLA rod was subtracted from the gel block geometry to produce a contact surface between the gel block and the PLA rod. Finally, two circles of 1 cm diameter were drawn on both sides 3 cm from the midline of the PLA rod to represent the locations of the actuator and the accelerometer in the simulation software. This procedure was repeated for each of the phantoms used in the real-life measurements to produce equivalent geometry for the finite element model (Figure 3).

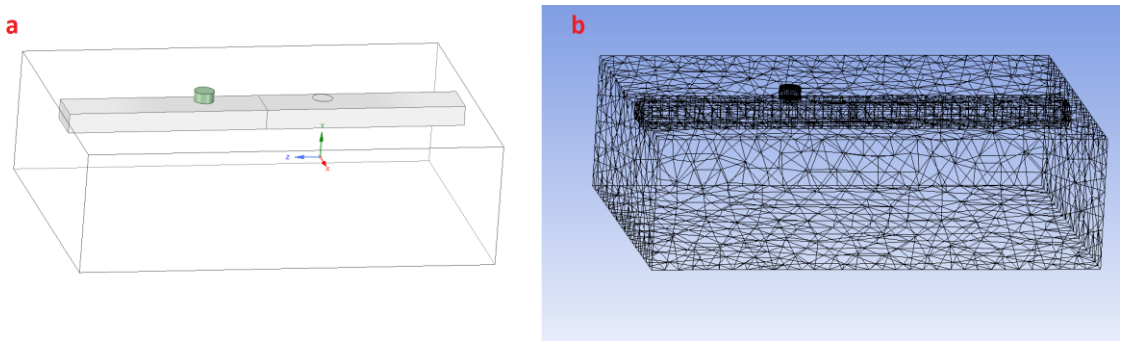

Figure 3. 3D model created for the phantom in SpaceClaim (a) and after meshing in ANSYS (b).

ANSYS Mechanical Workbench was used to create a new project. First analysis type included in the project was Static Structural which would allow for possible preloading of the system for Harmonic Response analysis which was linked to it. Materials for PLA and Clear Ballistics gel were created in the Engineering Data and the values for Young's modulus, Poisson's ratio and density obtained from the measurements and literature were added. Linked Static Structural and Harmonic Response systems were created for each of the geometries created in SpaceClaim.

The systems were opened in ANSYS Mechanical and the individual geometries such as the gel block, the PLA rod and the actuator head were assigned materials and the geometry was meshed. Different mesh sizing options were experimented with to find coarsest setting which would produce similar simulation results to a fine mesh. Simulation accuracy improves when the number of elements is increased but at some point it results in diminishing returns with exponential increase in computational requirements. Fixed support was applied as a boundary condition on the bottom of the blocks to represent the block resting on a table like in real-life measurements. Sinusoidal force was applied in the Harmonic Response analysis on the actuator head and acceleration frequency response was read from both the actuator head and the surface where the accelerometer would be placed upon.

The Harmonic Response analysis requires density and some form of elastic modulus as material properties (Table 2) and Stiffness and Mass coefficients for damping of the system. These were determined experimentally by comparing the results of the simulation to results of the measurements. Table 2. Material properties for the materials used in the phantom

3.2 Cadaver measurements

Vibration measurements from an actual cadaver were obtained for this thesis. The cadaver was that of a 68-year-old male. He was 174 cm tall, weighed 57 kg and six days post mortem. Juha Hautalahti, a cardiac surgeon, performed the preparation of the body, the sternotomy surgical procedure and the vibration measurements while I and Atte Joutsen

were assisting with the data acquisition, equipment and taking notes of the measurement process.

The surface of the thorax was cleaned and steel wires were inserted between the ribs 5 and 7 about 15 cm away from the midline of the sternum. These wires were later used to create a gap between the sternal halves by pulling on them with a cargo strap. The cleaned thorax was covered with OPSITE film which is a transparent, adhesive film dressing. This was done for hygiene purposes when working with a cadaver.

The measurement points were marked on the OPSITE film with a marker pen on both sides of the sternum 3 cm from midline at the level of ribs 2, 3 and 4. These marks would be used to place the actuator and the accelerometer on the same measurement positions every time.

The starting temperature of the cadaver was 16 ºC. The first measurement was done on the intact sternum. Two sets of 15 measurements were done on level of ribs 2, 3 and 4. Multiple measurements are done so outlier results can be excluded. As the actuator used a solenoid to produce the vibration stimulus it heated up and was cooled down every 15 measurements with cold spray. The vibration measurement device saves the data on a USB memory stick and after complete set of measurements from each rib level the data was copied to a laptop and checked with MATLAB.

After the data from the measurement of the intact sternum was verified the cardiac surgeon started the sternotomy procedure. An incision was made along the midline of the sternum and the thickness of the soft tissues was measured with a caliper at rib levels 2, 3 and 4. The thickness of the soft tissues was 5 mm at the level of the 2nd rib, 5 mm at the level of the 3rd rib and 4 mm at the level of the 4th rib.

Following the measurements of the intact sternum the sternum was divided with an oscillating saw. The cargo straps were tightened and the sternal halves pulled apart. 10 mm wooden spacers were inserted between the sternal halves to make applying the number 7 Ethicon steel wires easier. Two wires were put through the manubrium and the rest of the wires were tightened around the body of the sternum at the level of ribs 2 to 6. The gap between the sternal halves was filled with Bluescan Ultraschall Gel to simulate presence of interstitial fluid and blood. The wooden spacers were removed and the incision was sutured close in single tissue layer. The distance between the measurement point markings was checked as in some previous cases it had changed as result of the suturing. Two sets of 15 measurements at rib levels 2, 3 and 4 were done as previously. After the measurements the wound was opened and the gap was verified to still being 10 mm as specified.

To simulate a smaller 5 mm gap pair of 5 mm wooden spacers were inserted between the sternal halves and the sternotomy closure steel wires were tightened until the gap closed down to 5 mm. The spacers were removed, the wound was closed with single layer suture

and the markings were checked as before and the measurements were repeated in two sets of 15 measurements at rib levels 2, 3 and 4. The wound is then opened and the gap is verified to still be 5 mm.

For the last set of measurements, the sternotomy closure steel wires were tightened so that the sternal halves were tightly pressed together. The wound was sutured close and the markings were checked again. The two sets of 15 measurements were repeated at rib levels 2, 3 and 4. The temperature of the cadaver was 20 ºC by the time the measurement session was finished.

Finally, the cadaver was prepared for obtaining a CT-image of the sternum with 10 mm gap between the sternal halves by opening the wound once more, replacing the steel wires and putting in the 10 mm wooden spacers to hold the sternal halves apart. The wound was then sutured close.

At the end of the measurement session data for intact sternum, sternum with 5 mm and 10 mm gaps and sternum with proper tight closure were obtained.

3.3 Cadaver upper thorax segmentation

3.3.1 Image acquisition

The image sets were acquired with GE Medical Systems LightSpeed RT16 CT-scanner. Image sets were acquired in helical scan mode. Imaging parameters of the scan are included in Table 3.

Table 3. Imaging parameters

Property	Value
Slice thickness	0.625 mm
Number of slices	2342
Exposure time	1281 ms
X-ray tube current	147 mA
Tube potential	120 kV
Rows	512
Columns	512
Voxel spacing	x: 0.793 / y: 0.793 / z: 0.325

The image set with intact sternum was acquired one day before the measurement session and the image set with 10 mm separation between sternal halves was acquired one day after the measurement session.

3.3.2 Image segmentation

Images were segmented using ITK-SNAP segmentation software. Before the DICOM image sets were imported to ITK-SNAP slices containing information not relevant to this project were removed from the image set. Removed slices included the pelvic region. As the main area of interest in this work was the sternum and tissues near it the segmentation area was limited to volume containing frontal half of the thorax starting from neck and ending about 7 cm below the xiphoid process. This volume included all true ribs and costal cartilage connected to them. Curve-based contrast adjustment was used to obtain optimal contrast between different tissue types.

As the DICOM set was from a CT image the soft tissue contrast was not good enough to tell apart individual muscles or ligaments. Tissues were segmented in seven different groups; muscle, connective tissues and internal organs in one group, adipose tissue, cortical bone, cancellous bone, cartilage, lungs and skin. Additionally, the air around the thorax was segmented to aid in segmentation of skin. An individual label was created for each tissue type or group of tissues.

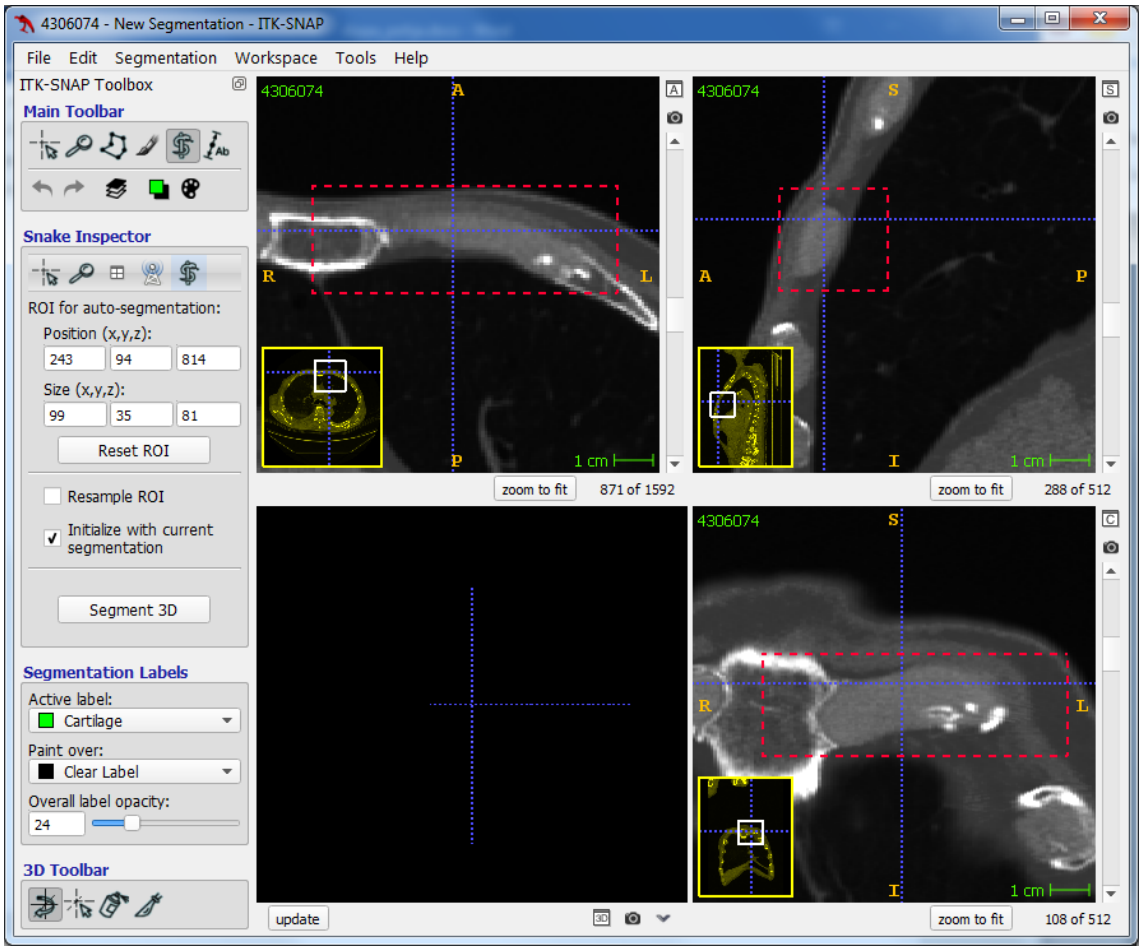

Figure 4. Setting ROI box for automatic segmentation of 3rd costal cartilage from the left side of the body.

Segmentation of tissues was started from cortical bone with ITK-SNAP's region competition snakes automatic segmentation tool. Clavicles, ribs and pieces of sternum were individually segmented by limiting the volume containing the tissue of interest, in this case an individual bone, with region of interest (ROI) tool. Figure 4 illustrates how the ROI box is set for 3rd costal cartilage form the left side. Pre-segmentation mode was set to "Thresholding" in which the Hounsfield Unit (HU) threshold values was set so that only the tissue of interest was clearly visible from the image (Figure 5 a). In next step seed points for the region competition snakes were added to the image (Figure 5 b) and snake algorithm settings governing the region competition force and smoothing force were set. Automatic segmentation was begun (Figure 5 c and e) and the results were monitored in real time during the progression of the region competition snakes (Figure 5 d and f). If the results were undesired, for example the snake didn't propagate to all tissues of interest or it leaked to other tissues, the threshold values, seed points and algorithm settings were adjusted until the desired results were obtained (Figure 5 g and h).

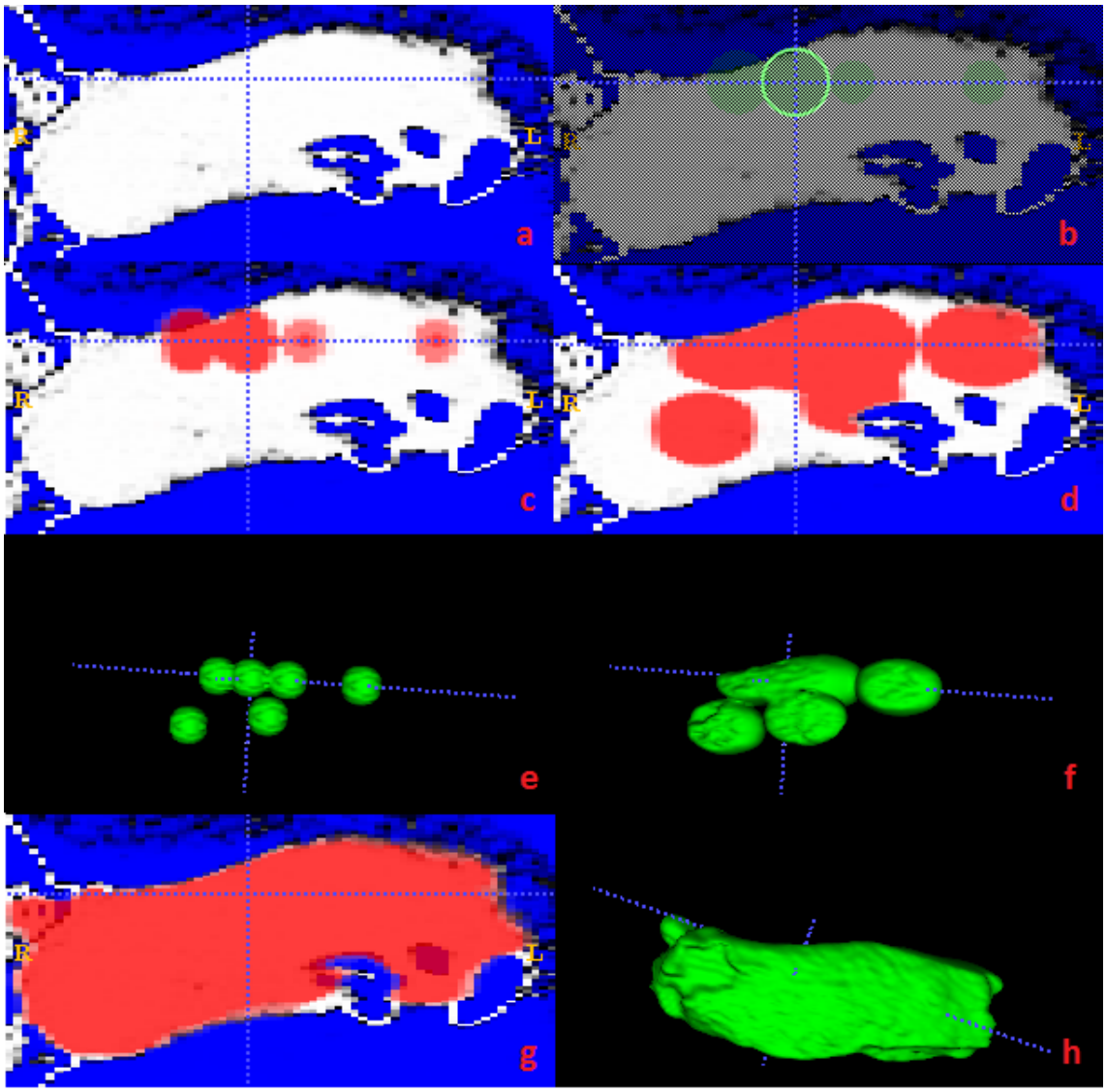

Figure 5. Automatic segmentation process of 3rd costal cartilage from the left side of the body from anterior perspective. (a) Threshold settings are adjusted so the cartilage is highlighted from rest of the image. (b) Setting seed points for the automatic segmentation algorithm. (c) & (e) 2D and 3D views of the seed points. (d) & (f) Automatic segmentation progressing. (g) & (h) Finished result of automatic segmentation. Note that part of the cancellous bone in the sternum was included in top left portion of (g) and on the lower right side the calcified parts of the cartilage were not included as their HU values in the image exceeded the threshold values for the automatic segmentation. These were later fixed manually.

The results of automatic segmentation were inspected, and problem areas were repaired and finished manually. In segmentation of cortical bone, the image resolution proved to be a problem since the bone thickness in the ribs was close to the voxel dimensions in some areas. This caused some areas of the cortical bone to be not segmented at all with the automatic segmentation algorithm. In these cases the segmentation was manually finished using “Paintbrush Mode” in ITK-SNAP. Other problem areas requiring manual repair were calcified volumes in costal cartilage which had the same HU values in the CT image as actual cortical bone. In these cases the automatic segmentation labeled calcified

cartilage as cortical bone and the demarcation between cortical bone and calcified cartilage was visually determined from the CT images and manually corrected with paintbrush tool.

The cancellous bone and bone marrow were segmented as one label. This segmentation was done completely manually because the automatic segmentation algorithm would constantly spill over to other tissues which had similar HU values in the CT image. It did not completely fill the space inside the cortical bone as the contrast difference between cortical and cancellous bone was quite big and this resulted in voxels along the demarcation line with HU values being average between cortical and cancellous bone. These two factors made complete manual segmentation of cancellous bone and bone marrow necessary. This was done with the paintbrush tool with the brush set to paint a three-dimensional volume to make it possible to segment multiple slices at the same time.

Costal cartilage was segmented after bones were finished. This was done automatically by setting a ROI volume around the individual piece of cartilage to be segmented and adjusting the threshold HU values so that only the piece of cartilage in the ROI volume was visible. As the HU values of the cartilage were close to the HU values of muscle tissue there was some spillover of the automatic segmentation to the muscle tissue. This along with areas of calcified cartilage which was not included in the automatic segmentation was fixed with manual tools.

To help with the segmentation of the soft tissues the air around the body was segmented with the automatic tools to provide a boundary for the skin as the skin itself had so similar HU values to the underlying muscle tissue that automatic segmentation of the skin was not possible. The skin was manually drawn to depth of approximately three voxels from the boundary of the air surrounding the body.

The muscle, fat and lung tissues were then segmented separately by using the automatic tools. As other tissues with similar HU values to muscle tissue were already segmented the automatic tools produced results with minimal need for manual correction. Heart, liver and major blood vessels were included in the segmentation of muscle tissue. Fat and lung tissues were segmented with the same method.

When all the tissues of interest were separately segmented it was noted that the automatic tools left some individual voxels unlabeled in the boundaries of tissues with significantly different HU values, such as the boundary of fat and cortical bone or lung and muscle or cortical bone. These defects were manually repaired slice by slice. The segmentation was also rendered in 3D to inspect for defects and to simplify the segmentation by removing small floating islands of tissues embedded in other type of segmented tissue.

It was later noted that including all the different tissue types segmented in the finite element model would increase the complexity and computational requirements of the model

too much and a segmentation was created where skin, muscle and fat tissues were lumped to general soft tissue and cortical and cancellous bone were combined as one.

This entire process was repeated for both the CT image of the intact sternum and the sternum with 10 mm gap. The latter was a bit more complex with the inclusion of the fluid in between and behind the sternal halves and steel wires holding the sternum. It also required much more manual clean up as the steel wires produced significant artifacts on the CT image.

Finally, the individual segmented geometries such as soft tissues, bone and cartilage were exported in STL format for conversion to finite element model.

3.4 Building the finite element model from the segmented geometry

3.4.1 Importing the segmented geometry to ANSYS

ITK-SNAP generated the STL files from the voxel data with marching cubes algorithm [55]. This resulted in a surface mesh with very rough surface. The STL files were imported to MeshLab for initial polygon count reduction and smoothing (Figure 6 a). MeshLab includes “MC edge collapse” tool which is designed for polygon count reduction and smoothing for meshes created by marching cubes algorithm (Figure 6 b). This was first applied to the imported STL files followed by Taubin smoothing algorithm which was used to further smooth the rough surface meshes (Figure 6 c). Taubin smoothing was used as a smoothing method because it does a good job of preserving original mesh boundaries without deformation or shrinkage [56]. After these operations the polygon count of the surface meshes was still very high, over one million polygons per segmented tissue geometry. As the computational resources available were rather limited a further reduction of the polygon count was required. Unfortunately, the Quadric edge decimation tool of MeshLab didn’t work for polygon count reduction for these geometries as it produced lots of errors like holes, non-manifold edges and self-intersecting faces.

As the polygon count could not be further reduced in MeshLab Autodesk Netfabb was used for that task. Autodesk Netfabb has re-meshing tool which allows for reduction of polygon count of a surface mesh with user specified maximum allowable deformation of the mesh (Figure 6 d). This setting was set to 0.5 mm which is close to the voxel size of the original CT image stack. The target polygon count was set to lowest possible. There were still some errors in the meshes and they were fixed with the repairs tools of Netfabb. After that each individual costal cartilage and rib were separated to their own files.

As a result of smoothing and polygon count reduction the meshes had distorted slightly and the meshes of the costal cartilage no longer perfectly fit the corresponding ribs and the sternum. These gaps were fixed by selecting the areas of each cartilage mesh that would touch bone and by extruding them by roughly 1 mm. Now the cartilage pieces were slightly intersecting with the ribs and the sternum but the gaps between the bones and the cartilage were filled.

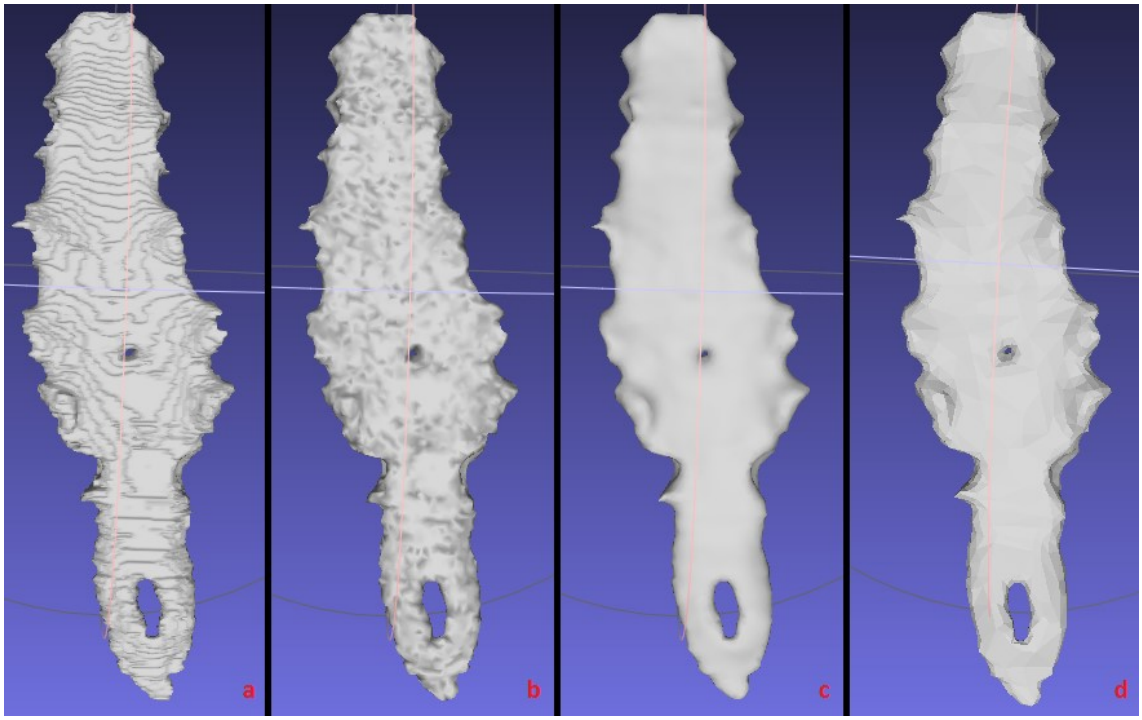

Figure 6. Smoothing and polygon count reduction of the surface mesh of the body of the sternum. (a) Illustrates how the surface mesh of segmented sternum exported from ITK-SNAP looks like. (b) Mesh after MC edge collapse filter. (c) Mesh after Taubin smooth operation. (d) Mesh after reduction of polygon count in Netfabb.

The lungs and other soft tissues had their meshes and they were prepared in with the same methods in MeshLab and Netfabb to smooth the surfaces and to reduce the polygon count.

Once the surface meshes had been prepared in Netfabb they were imported to ANSYS SpaceClaim. SpaceClaim allows for importation of STL format meshes and direct conversion to faceted solids. An ANSYS Workbench project was also started so that it could be verified that finite element meshes can be generated from the solid format files. The first part to be imported was the surface mesh for combination of all segmented tissues as Boolean operations could be used to subtract other parts like bones and cartilage from it to provide accurate fit between the different domains. Individual ribs, costal cartilage, the manubrium and the body of the sternum were imported one by

one to SpaceClaim and inspected for problems like geometry errors and too small faces. If any errors were found, they were fixed in Netfabb and imported to SpaceClaim again.

When for example the first rib from left side, its corresponding costal cartilage and manubrium had been imported and verified in SpaceClaim they were opened in ANSYS Design Modeler in the ANSYS Workbench project. There a Boolean operation was performed subtracting the rib and manubrium from the costal cartilage as they were slightly intersecting from the gap filling operation performed in Netfabb. This Boolean operation removed the intersecting geometry from the cartilage piece. Then another subtraction was performed to subtract the bones and the cartilage from the solid mass presenting all tissues.

After importing the parts to Design Modeler and performing the Boolean operations a Static structural analysis was added to the Workbench project and the imported solids were used as the geometry for the analysis. A finite element mesh of the geometry was created, and a simulation of force applied on it was run to see that it was working. If the model was working correctly in the meshing and simulation the next set of ribs and cartilage were imported to SpaceClaim and to Design Modeler and then added to the Static structural analysis and the meshing and simulation were performed again to see if it was still working. If any errors were present the offending geometry was identified and corrected in Netfabb and then imported back to SpaceClaim and Design Modeler again.

This process was repeated until all the 16 ribs and their corresponding costal cartilage, sternum and lungs were fitted into the soft tissues and the geometries were meshing correctly and the Static structural simulation could be performed on them without errors.

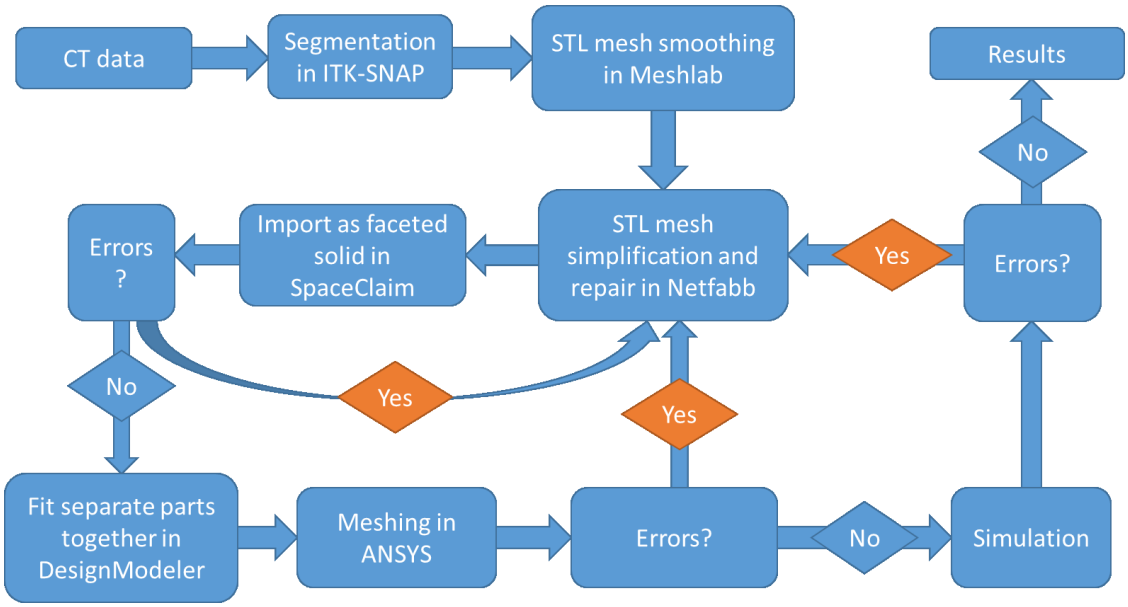

Figure 7. Flowchart of the geometry importation process to ANSYS.

3.4.2 Material properties for the finite element model of the thorax

Material properties of human tissues for the finite element model of the thorax were obtained from literature. As the tissues were modeled as isotropic and homogeneous in this case the required material properties for the simulation were density, Young's modulus and Poisson's ratio. The tissues that were segmented separately were skin, fat, muscle and internal organs, cortical bone, cancellous bone, lungs and cartilage. When building the model, it was noted that separating all the soft tissues and having two different bone types would cause too many geometry errors and increase the computational requirements too much so the model was simplified by lumping all soft tissues together as homogeneous mass and by combining the cortical and cancellous bone into one.

Table 4. Material properties for different tissue types

Tissue	Density (g / cm³)	Young's modulus (MPa)	Poisson's ratio	Literature source
Cortical bone	1.99	15100	0.33	Murphy et al. [57]
Cancellous bone	0.86	142	0.45	Furusu et al. [9, 57], Murphy et al. [57]
Costal cartilage	1.5	24.5	0.4	Furusu et al. [9, 57], Murphy et al. [57]
Muscle, adipose tissue and skin as homogeneous viscus	1.0	1	0.3	Furusu et. al [9]
Lungs	0.3	0.002	0.4	Liu and Tschumperlin [59], Wells [60], Rhodes et al. [61]

When it comes to material properties of human tissues in literature there was a lot of variation depending on the condition of the test samples, age of the person or animal the samples were obtained from, the site and bone the samples were obtained from and the measurement technique [57]. For example in case of cancellous bone the reported Young's modulus varied between 0.76 GPa and 20 GPa in published research articles [58]. The material properties used in this thesis were mostly obtained from "Handbook of biomaterial properties" by Murphy et al. [57] and from the THUMS occupant model by Furusu et al. [9]. Material properties for lung tissue had to be obtained from multiple sources [59-61]. The material properties for different tissues used in this thesis and sources for the material properties are composed in Table 4.

3.5 Simple model for testing simulation parameters

3.5.1 Model 1

As the PC used to work on this thesis had rather limited resources (Core i5 3470, 32GB RAM, 500GB SSD) and the finite element mesh generated from the segmented geometry had about 800,000 elements even with coarse meshing settings it was necessary to build a simpler representation of ribs, cartilage, sternum, lungs and soft tissues for testing of simulation parameters. This model was drawn in ANSYS SpaceClaim.

First the cross section of the shape representing soft tissues was drawn on a 2D plane. That geometry was then extruded to produce a 3D object. Then using the surface of soft tissue geometry as a guide three pairs of ribs were drawn 3mm below the surface of the soft tissue geometry. Each of the ribs were 6 mm thick and 20 mm wide and followed the curvature of the soft tissue surface. A rectangular geometry representing the sternum with dimensions of 150 mm by 30 mm by 6 mm was placed in the middle of the soft tissue block just 3 mm under the surface. Cancellous bone was created by subtracting geometries with dimensions 1 mm less on each side from the geometries representing bones. This created a 1 mm thick shell representing the cortical bone on the ribs and the sternum and internal volumes of cancellous bone.

Geometries representing cartilage were created to bridge the gaps between the ribs and the sternum. This was done in the same way as creating the ribs, with geometries following the curvature of the soft tissue surface, beginning from the ends of the ribs and terminating in the sternum.

Lungs were added drawing their cross section on a 2D plane and by extruding them to fill the area below the ribs, cartilage and sternum. Finally, probes were added on top of each cartilage piece 3 cm from the midline so a frequency sweep excitation could be applied on the model in ANSYS Mechanical finite element software.

Different kind of defects were created on the geometry representing sternum and to the soft tissues surrounding it. The sternum was cut in two from the midline and the model was simulated with no gap between the halves and with a 2mm defect between them. Healed sternum was simulated by filling the gap with cortical bone.

Fitting all the parts together was finalized in ANSYS DesignModeler and the geometries were then imported in ANSYS Mechanical and meshed successfully. Different meshing settings were tested to find balance between accuracy of the simulation and the computational requirements. Harmonic Response analysis was performed on the geometries with a frequency sweep from 20 Hz to 2000 Hz with 10 Hz resolution.

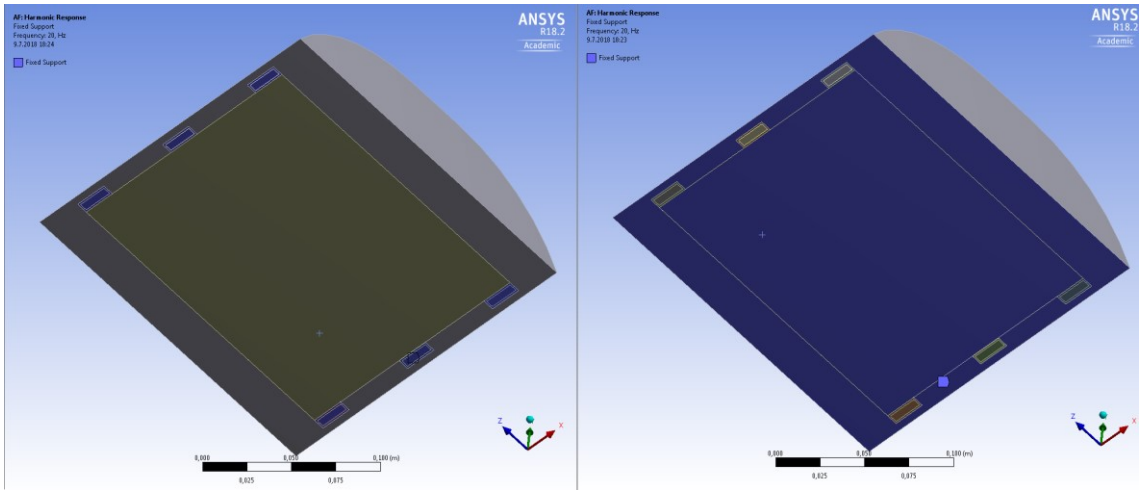

Figure 8. Fixed support on the ends of the "bones" on the left and fixed support on the soft tissues on the right.

In real life measurements the subject is supported by the surface he is lying down on. Since both the segmented geometry and the first simplified model only presented the anterior half of the thorax there was a question of where to apply the fixed support. It was decided to simulate the model with fixed support on ends of the “ribs” and with fixed support on soft tissues (Figure 8) to see if there was significant different between those two options.

3.5.2 Model 2

As the first simple model was tested in Harmonic Response analysis it was noted that the boundary conditions, especially the location of the fixed support had clear impact in the simulation results. If the fixed support was applied on the ends of the bone geometry the results were different to if the fixed support was applied on the soft tissue. Because of this another simple model was built based on measurements taken from the CT data. Thickness of the sternum, costal cartilage, ribs and other tissues were measured from cross sectional image at the level of the 3rd costal cartilage and the measurements (Figure 9)

were used to create rough 2D presentation of the sternum, costal cartilage, ribs, spine, lungs and other soft tissues. This 2D presentation was then converted into a 3D model by using extrusion tools in ANSYS SpaceClaim (Figure 10).

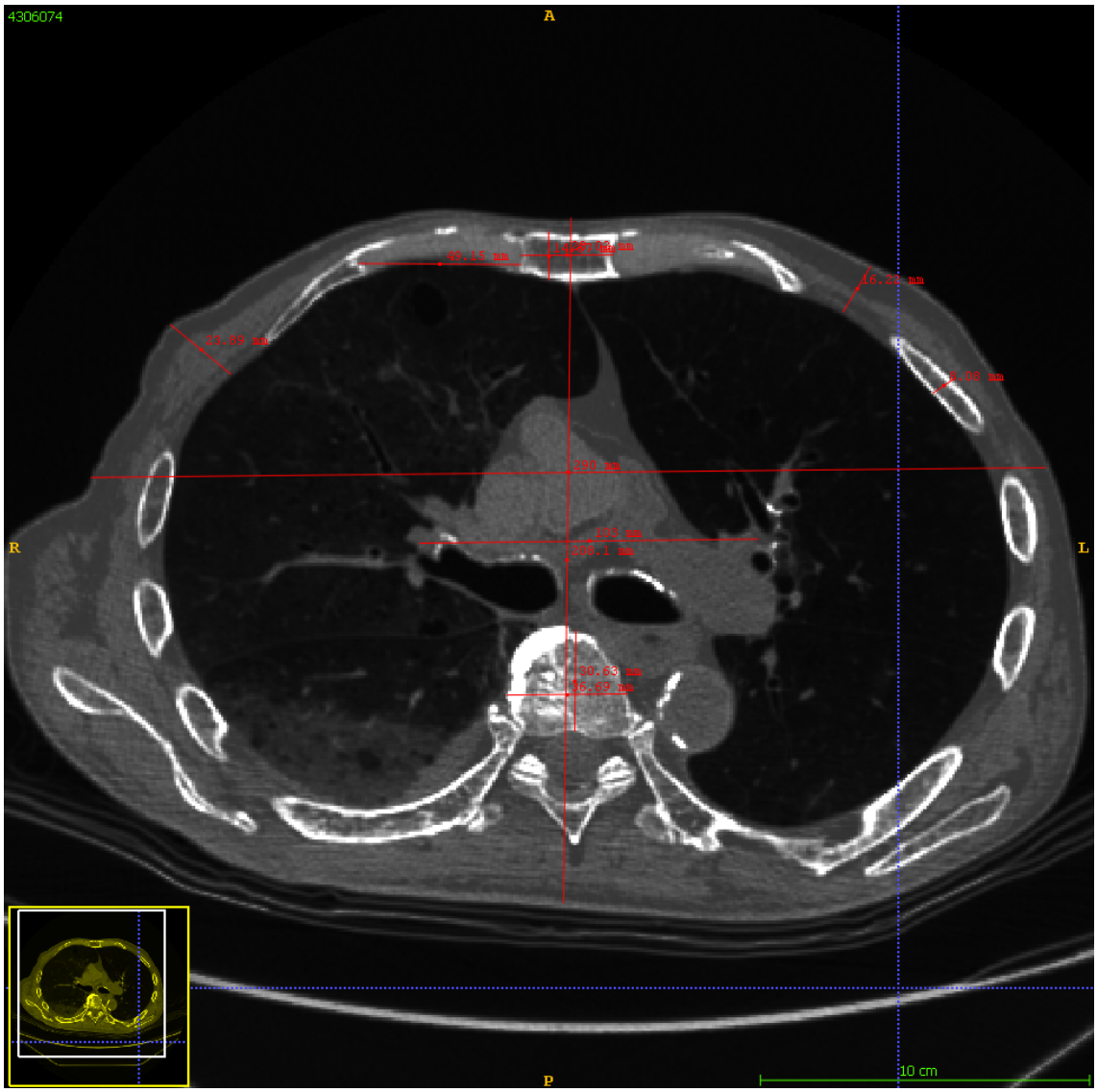

Figure 9. Taking measurements in ITK-SNAP.

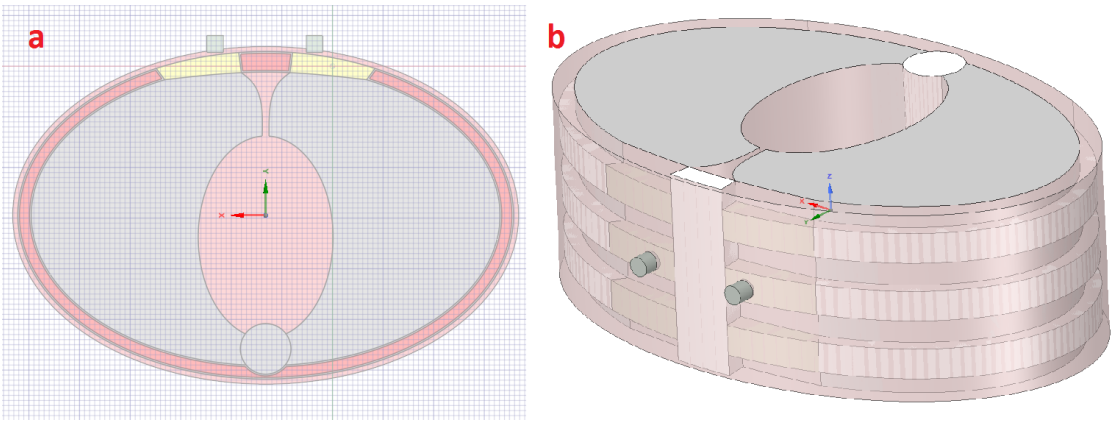

Figure 10. (a) Rough sketch based on the measurements. (b) 3D model created from the sketch.

3.6 Data analysis in MATLAB

The data measured from the phantoms and the cadaver was imported to MATLAB. Code written by Atte Joutsen for the project was modified and used to convert the .DAT output files of the vibration measurement device to matrices where each row of the matrix was raw data from one vibration sweep. As some of the vibration sweep raw data had trailing zeroes the matrices were shortened to get rid of them. Each matrix had raw data from 20-30 measurements depending on phantom that was measured. The amount of raw data per phantom varied a bit since some of the data had to be discarded as it was clearly faulty.

Each raw data segment held ~36000 samples and the sample rate of the measurement was 10 kHz. As the accelerometer of the vibration measurement device was not calibrated the raw data had a DC level which was removed by subtracting mean value of each vibration sweep raw data row from the values of the row. A fast Fourier transform (FFT) operation was performed for each row of the matrices and saved in a new matrix. A mean value of all FFT's for each phantom was obtained and single sided amplitude spectrum was calculated to get the mean frequency response of each phantom. Local regression smoothing (Loess) was used to obtain smoothed graphs of frequency response.

4. RESULTS

4.1 Phantom measurement and simulation results

4.1.1 Phantom measurement results

In the first measurement the phantom used had no PLA rod embedded in the synthetic ballistic gelatin (Figure 11). The synthetic ballistic gelatin mostly let through vibrations below frequency of 400 Hz with the maximum amplitude occurring at 148 Hz. Frequencies above 500 Hz were almost entirely attenuated.

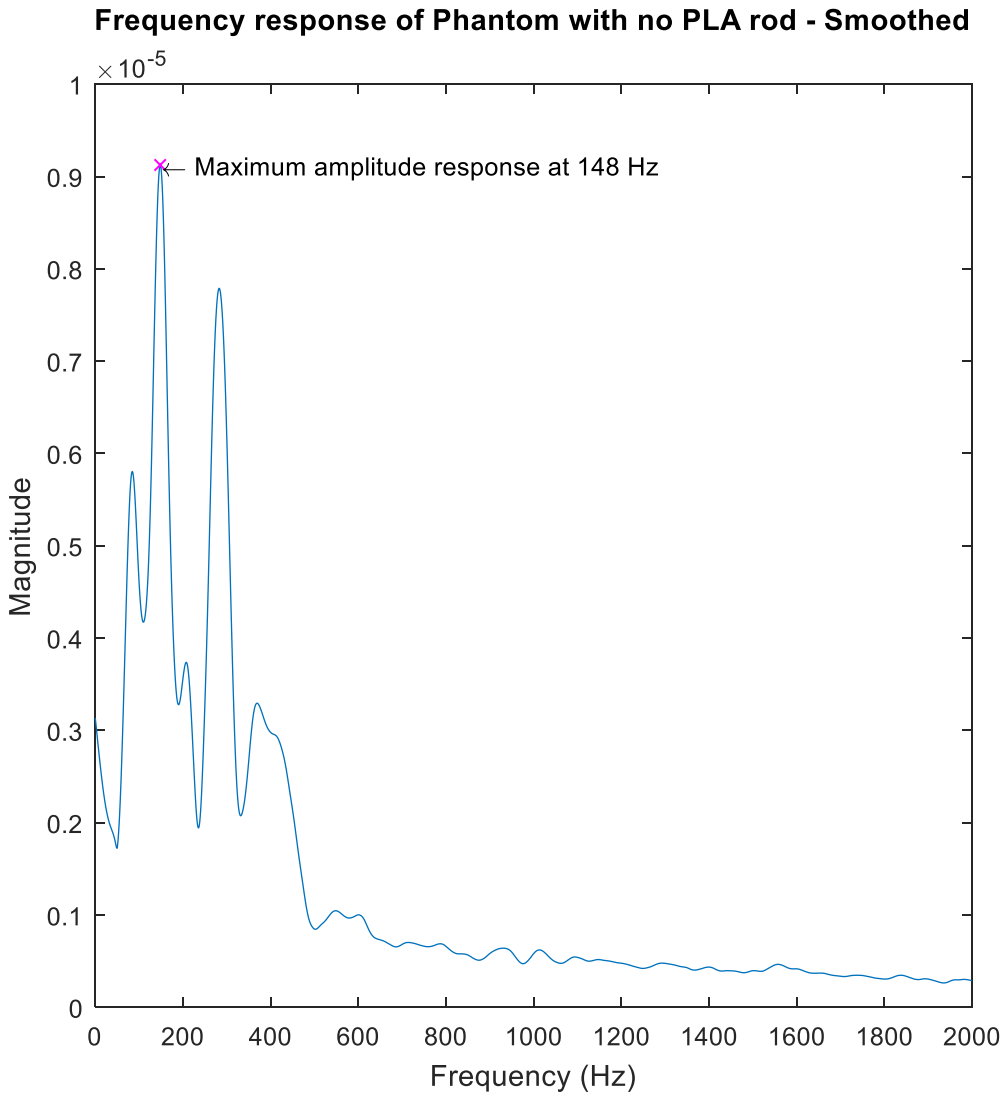

Figure 11. The gel block mostly let through frequencies below 500 Hz with maximum amplitude response occurring at 148 Hz.

When an intact PLA rod was embedded in the gel block (Figure 12) the amplitude response changed with maximum amplitude peak occurring at 485 Hz. This frequency was mostly attenuated in the block with no PLA rod embedded so the vibration is most likely conducted via the PLA rod from the actuator to the accelerometer.

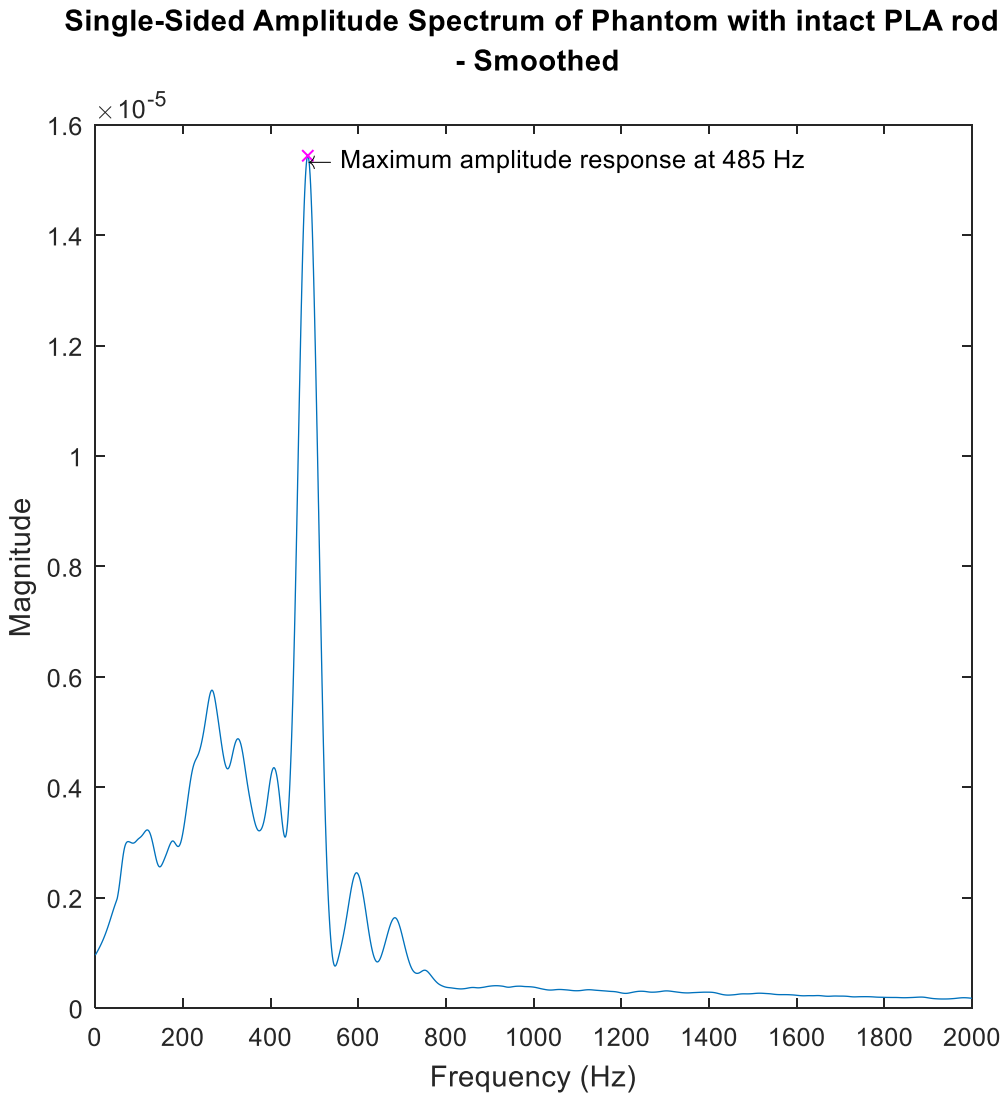

Figure 12. As the PLA rod is embedded in the gel block the frequency response changes with maximum amplitude response being present at much higher frequency.

When the PLA rod embedded in the gel block was cut in half (Figure 13) the frequency response doesn't change much from the intact PLA rod. The maximum amplitude response occurs at 454 Hz and the maximum amplitude is higher than with the intact rod the magnitude differences can be explained by the design of the actuator part of the vibration measurement device which makes it possible for the user to affect the measurement results. This and other reliability issues of the device are further discussed in chapter 5.1.

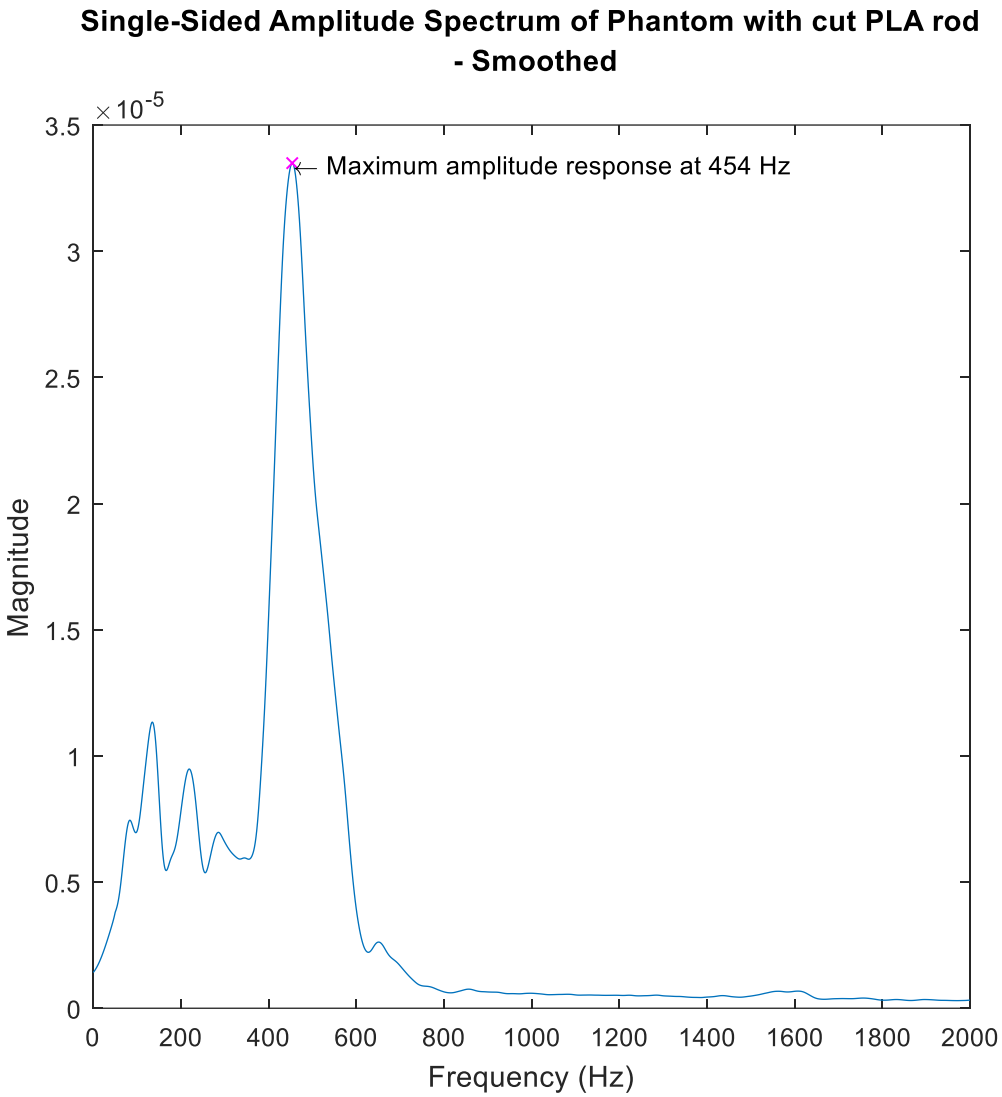

Figure 13. The frequency response with the cut PLA rod is similar to the intact PLA rod albeit with much higher maximum amplitude.

In the last measured phantom, the cut PLA rod was sutured back together with surgical steel wire used in sternotomy closures to determine if the steel wires have any noticeable effect in the vibration transmission (Figure 14). The maximum amplitude response occurs at 508 Hz and the response is very similar to the phantoms with intact and cut PLA rods.

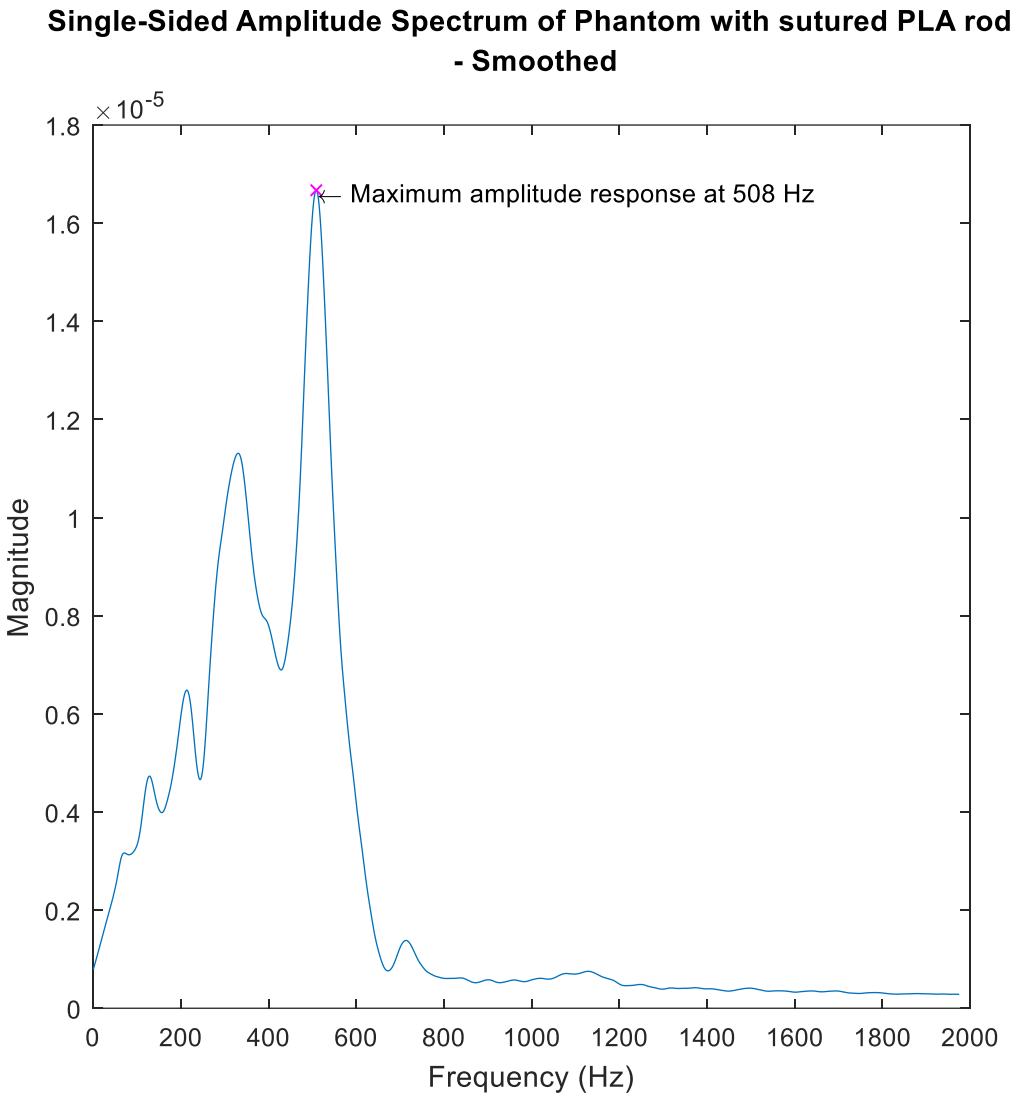

Figure 14. Frequency response of the phantom gel block with sutured PLA rod embedded is very similar to the phantoms with intact and cut PLA rods.

These results indicate that vibration measurement device can detect if an object with significantly different vibration transmission properties is present in the measured soft body. However, considering the reliability issues with the device (chapter 5.1) no conclusions can be made from the magnitude of the frequency response as the user can easily affect it by the way he holds the actuator. So, while the results from the phantoms with embedded intact, cut and sutured PLA rods show differing magnitude of the frequency response it's not possible use results like these to determine the nature of the defect present in the phantom.

The defect simulated in the phantoms was relatively minor as the ends of the cut PLA rods were in good contact with each other and well supported from all sides by the cast synthetic ballistic gelatin. This differs significantly from the extensive defects present in the cadaver measured in Chapter 4.2.1 (Figure 20).

4.1.2 Phantom simulation results

Models for the measured phantoms were created (chapter 3.1.4) and a harmonic response analysis was performed on them in ANSYS to obtain their frequency response to vibration on the same 20 Hz to 2000 Hz vibration sweep as in the real measurements.

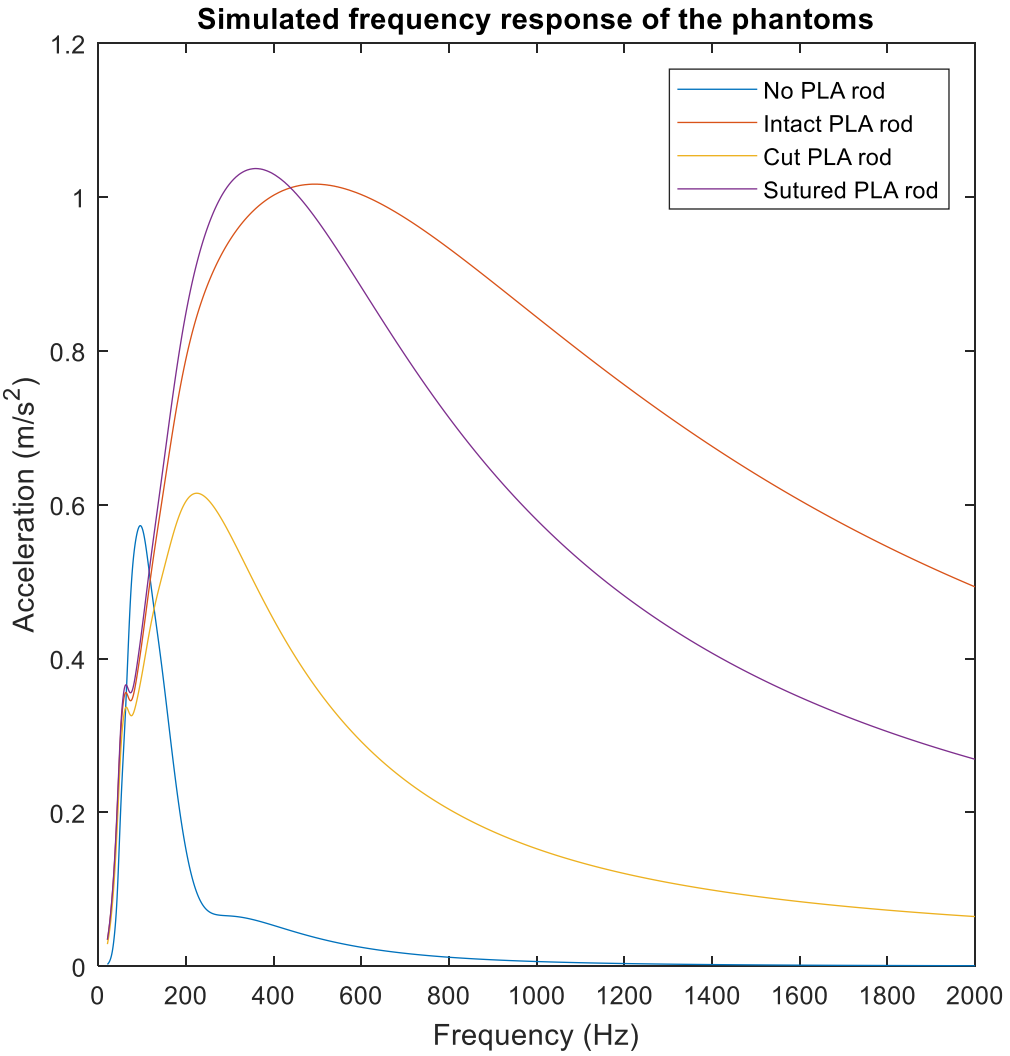

Figure 15. A harmonic response analysis was performed on models of the phantoms. Frequency sweep range was the same 20 to 2000 Hz as with the real measurements. Data was acquired at 10 Hz intervals.

Figure 15 displays the simulated frequency response of the phantoms. In comparison the measured results in Chapter 4.1.1 there is similarity in how the peak amplitude moves to lower frequency as the vibration has to pass through the soft tissue analogue but the absolute amplitudes differ from the measured results.

The harmonic response analysis simulation gives very similar results for phantoms with the intact and sutured PLA rods while cut PLA rod produces similar results to the phantom with no PLA rod at all. This result differs from the actual measured results as all phantoms with PLA rods in them produced similar results while phantom with no PLA rod was the odd one out.

It's likely that the damping coefficients of the modeled system weren't very accurate as there was no way to measure them from the actual phantoms and they had to be experimentally determined.

4.2 Cadaver measurement, segmentation and FEM results

4.2.1 Cadaver measurement results

The cadaver measurements were performed as described in Chapter 3.2 and the results were analyzed and plotted in the same way as in the phantom measurements.

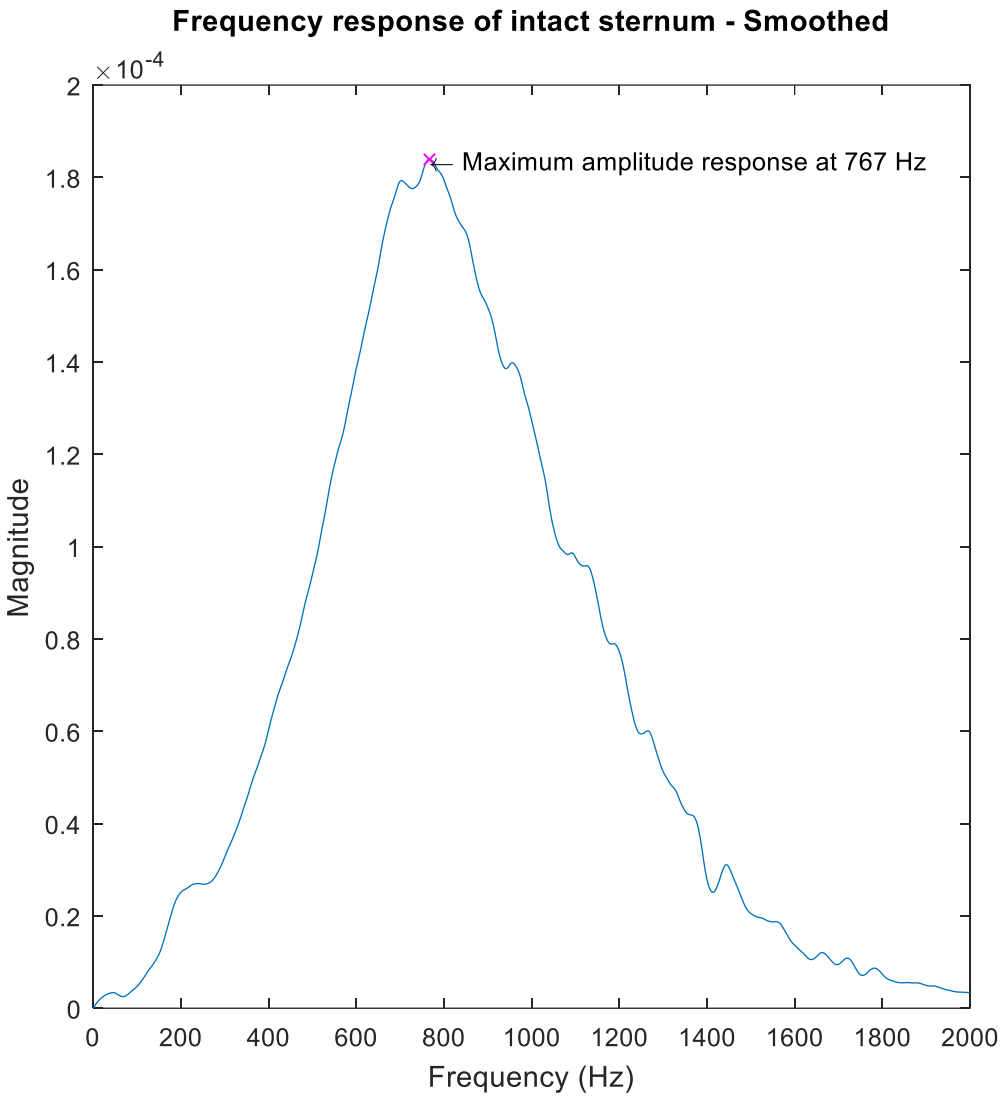

Figure 16. Frequency response of intact sternum.

In the case of the intact sternum (Figure 16) the peak frequency response occurs at 767 Hz. Not much vibration is conducted through the sternum at low or high frequencies. The peak of the frequency response is not as sharp as with the phantom and the frequencies going through the sternum are higher as with the phantom not much vibration was transmitted through after 600 Hz frequency was reached.

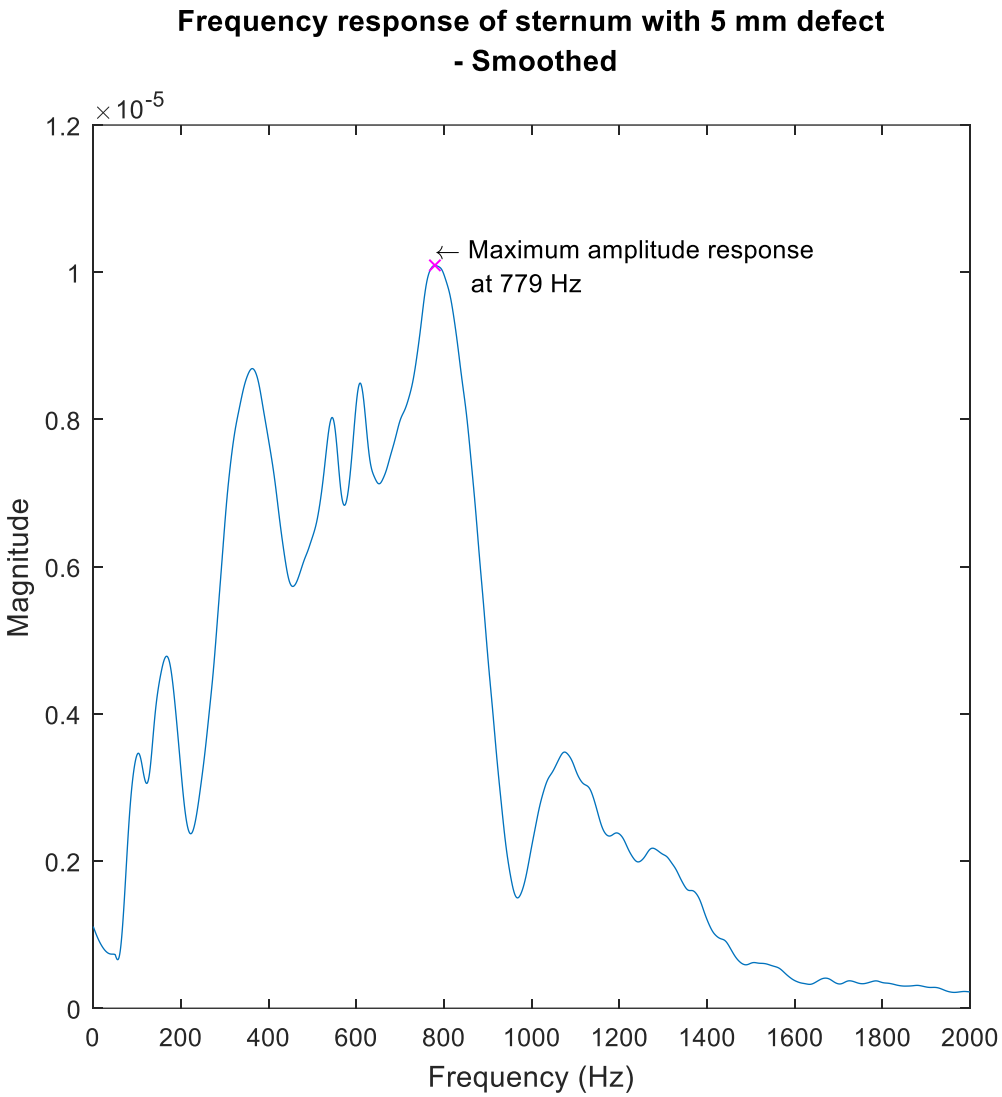

Figure 17. Frequency response of sternum with 5 mm wide defect on the midline.

When a gap of 5 mm was created in the sternum the peak frequency remains similar to the intact sternum but the amount of vibration reaching the accelerometer has dropped by an order of magnitude. This isn't likely just a measurement error like the magnitude differences in the phantom but a result of how extensive the defect was (Figure 20 has CT image of the defect with 10 mm gap).

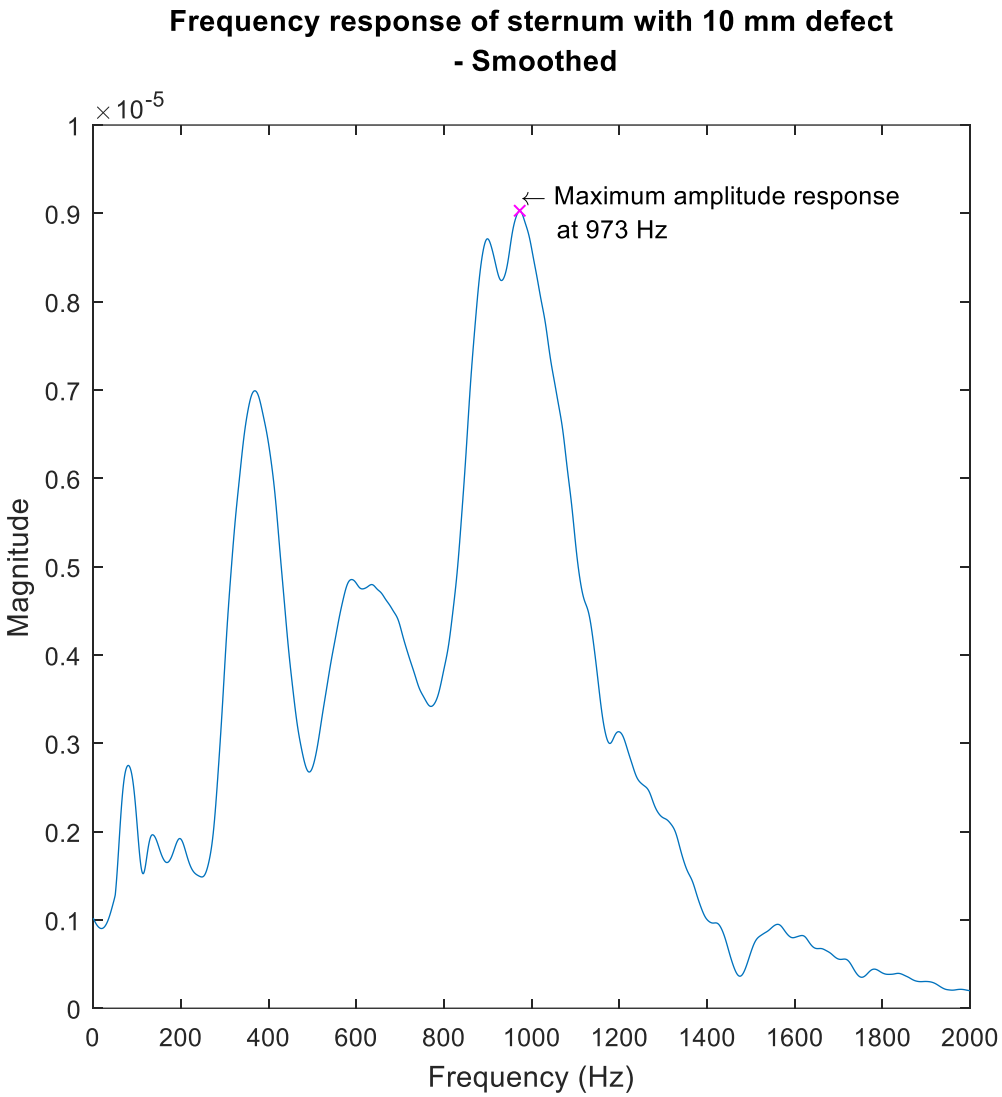

Figure 18. Frequency response of sternum with 10 mm wide defect on the midline.

In case of the 10 mm gap (Figure 18) the magnitude of the frequency response is similar to the 5 mm gap (Figure 17) and while the frequency response has shifted a little. The overall differences are so small that they might have been caused by the operator of the device as it was discovered with the phantoms that how the actuator and accelerometer are held affects the results.

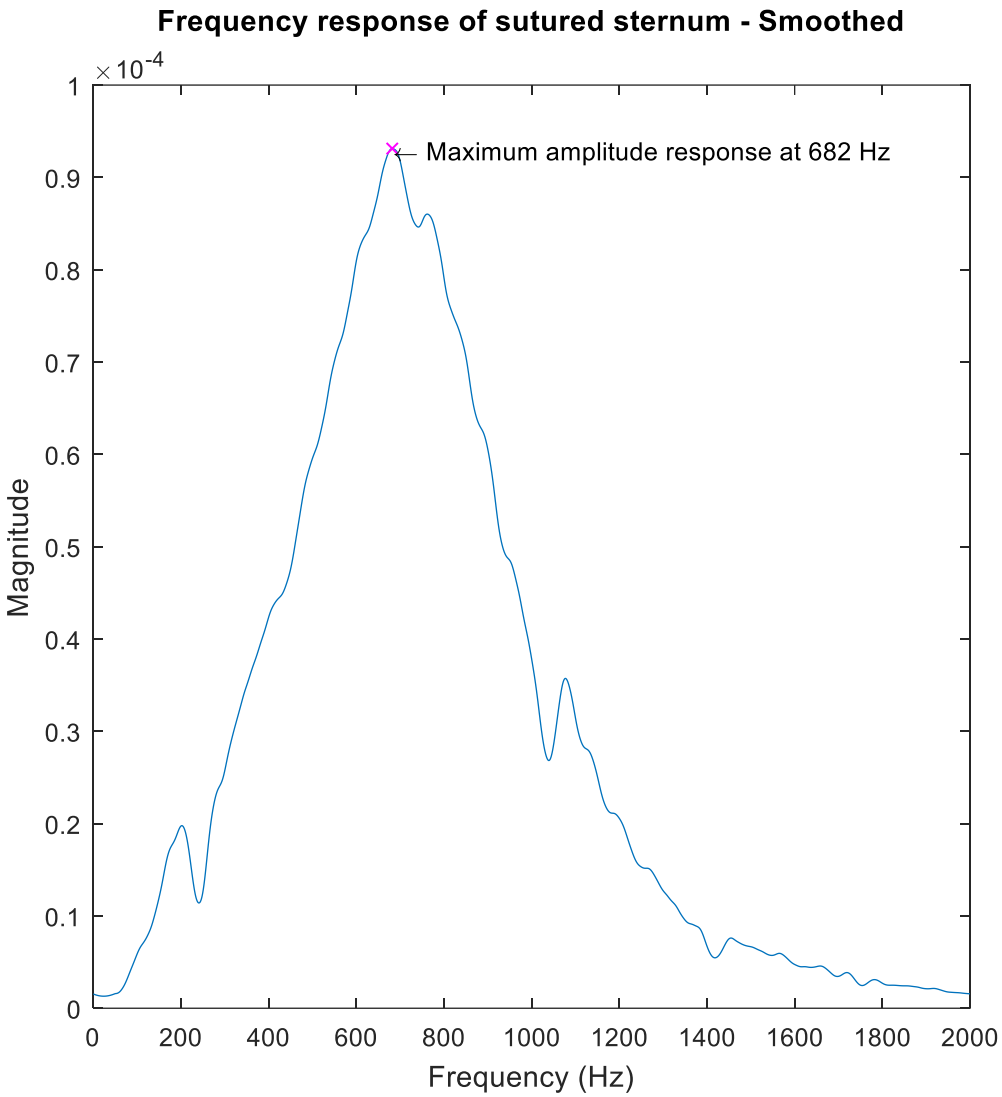

Figure 19. Frequency response of tightly sutured sternum.

After the sternum was sutured tightly back together the frequency response was order of magnitude higher (Figure 19) than with the 5 mm and 10 mm gaps. Overall, it's very similar to the frequency response of the intact sternum (Figure 16).

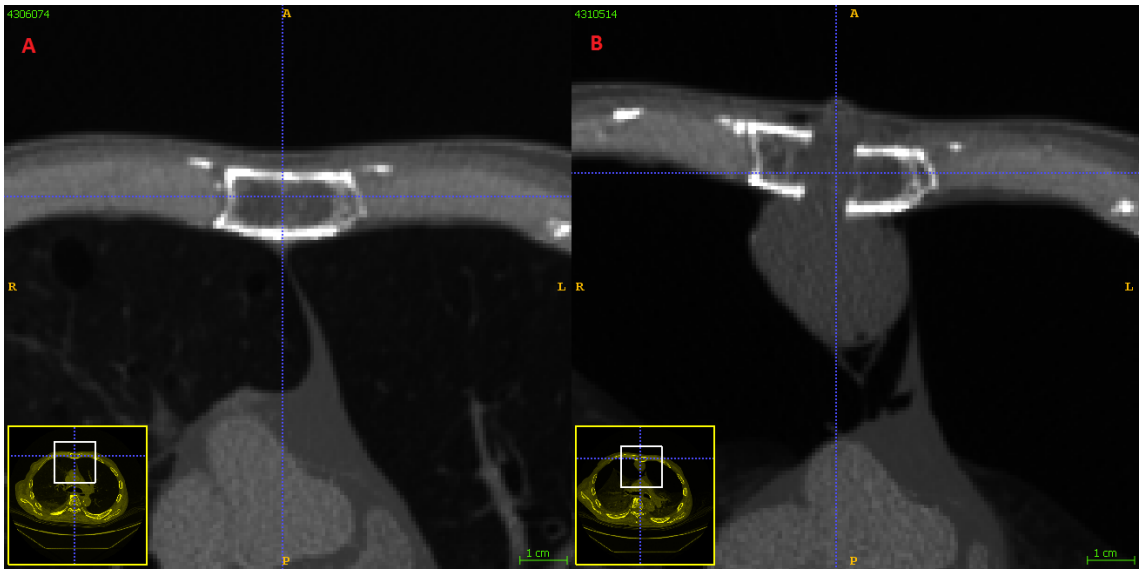

Figure 20. Comparison of intact sternum (A) and sternum with 10 mm defect (B) at the level of third costal cartilage. The defect extends to the posterior side of the sternum and the lungs have collapsed.

CT images of the cadaver were obtained with intact sternum and sternum with the 10 mm defect (Figure 20). The gap in the latter case was filled with ultrasonic gel as the cadaver no longer has any circulation and in a living body the defect would mostly be filled with intercellular fluids.

As the test subject had a body mass index (BMI) of 18.8 there was very little soft tissues on top of the ribcage and sternum. In addition, the soft tissue layer had an incision all the way through and was only held together by sutures. So, in case of both the 5 mm and 10 mm gaps in the sternum there was very little soft tissue to conduct the vibration and most of the defect is filled with the ultrasonic gel. When looking at the measurement results of the phantoms (Chapter 4.1.1) even the much stiffer synthetic ballistic gelatin conducts vibration poorly compared to a solid body. It's very likely that the ultrasonic gel is not conducting much vibration if at all.

4.2.2 Cadaver segmentation results

Area around the sternum was segmented from two CT data sets, one had intact sternum and one had sternum post-sternotomy with steel wire sutures and a 10 mm defect along the midline. Tissues segmented separately were cortical bone, cancellous bone, cartilage, skin, lungs, adipose tissue and rest of the soft tissues (muscle and internal organs). In the data set with post-sternotomy sternum the steel wires, air filling the collapsed lungs and the ultrasound gel filling the defect were also segmented. As the differentiation between different types of soft tissues in CT images can be rather poor many of the boundaries, for example cartilage to muscle, were approximated. Figure 21 displays the region segmented from both CT data sets.

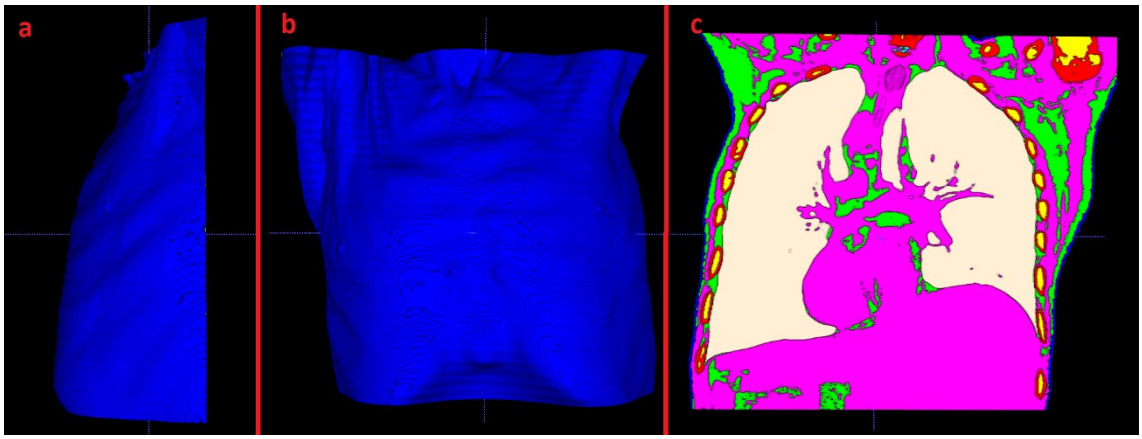

Figure 21. Region segmented from both CT images. Lateral view (a), anterior view (b) and posterior view (c) of the segmented region.

In Figure 22 and Figure 23 the soft tissues except the lungs are hidden and the difference between the intact sternum and the post-sternotomy sternum with the 10 mm defect are clearly visible. When examining the CT images during the segmentation process it was noticed that the lungs of the cadaver deflate when air gets between the pleura and the lungs when the simulated defect is created.

Figure 22. Skin, adipose tissue, muscle and internal organs hidden in the segmentation of intact sternum revealing the bones, cartilage and lungs.

Figure 23. Segmentation of the post-sternotomy sternum showing the collapsed lungs and extent of the defect.

As the CT data sets used in the segmentation were obtained from a cadaver it was not necessary to consider the radiation dose from perspective of patient safety and the image quality could be maximized. This made the otherwise difficult differentiation of soft tissues a bit easier than when segmenting CT images from a living patient and thus improved the quality of the segmentation a bit. There were still some issues with the boundary between the cartilage and muscle tissue for example and this is visible in the rough cartilage surfaces in Figure 22 and Figure 23 as in reality the surface of cartilage is smooth. Thickness of some features like cortical bone in ribs and the sternum was less than the width of a voxel in image in some points and those areas had to be manually approximated in the segmentation.

4.2.3 Finite element model of the thorax

A finite element model of the anterior half of the thorax was created (Figure 24) and successfully tested with some loads. The element count of the model was high (>800,000 tetrahedral elements) despite the rather coarse mesh. This resulted in excessive memory and disk space requirements when running anything but simple static analysis on the model.

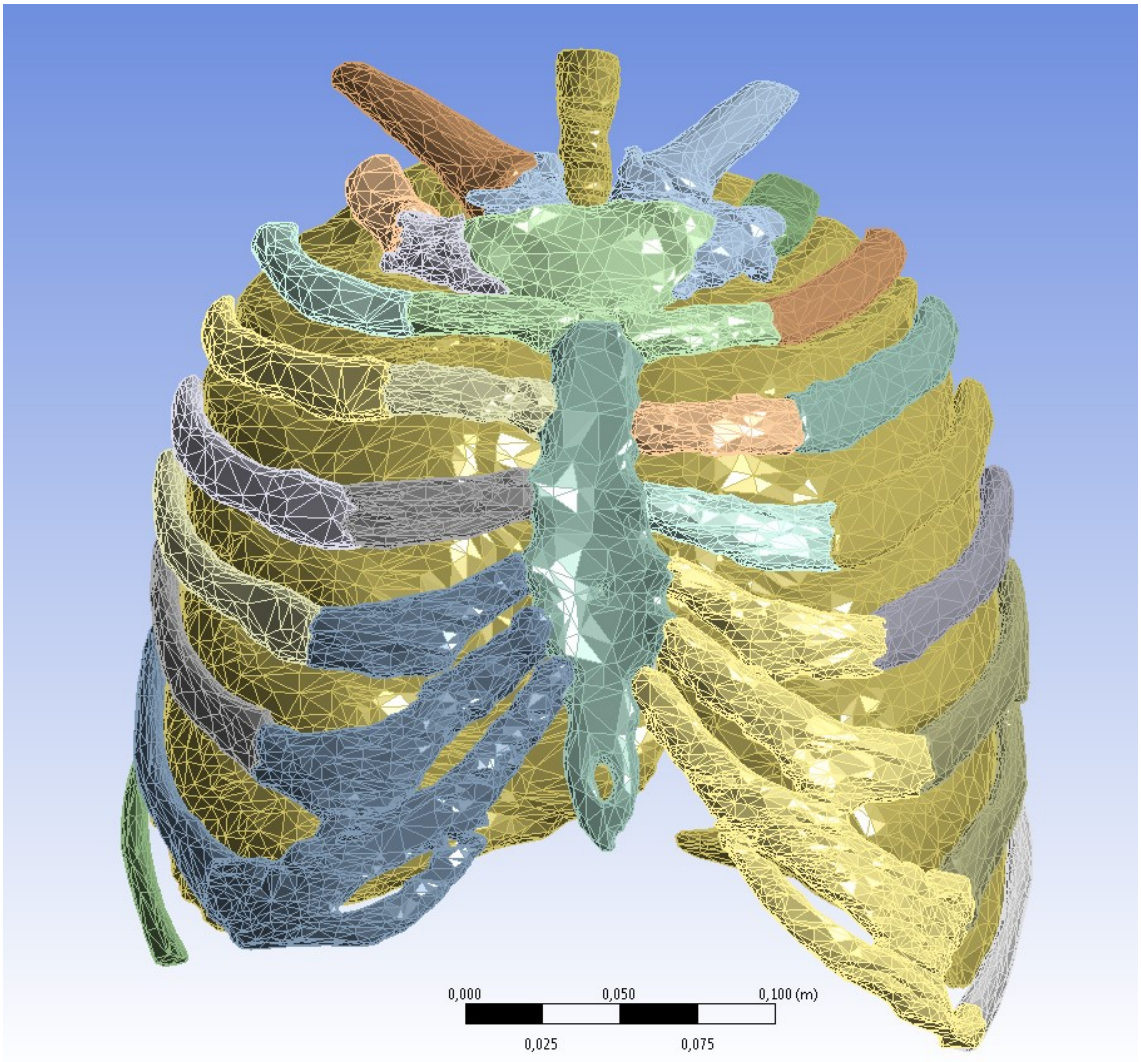

Figure 24. Finite element mesh of bones, cartilage and lungs. Soft tissues hidden for visibility.

The tissues were modeled as isotropic and linear. Bones were modeled as homogeneous tissue as including cortical and cancellous bone separately increased the number of elements to a point where the computational resources available were not enough.

As simulation problems were encountered with this model creating a Virtual Topology of the thorax model was attempted (Figure 25). In this approach the individual faces of the solid model were combined in ANSYS Workbench to larger continuous surfaces to avoid meshing problems with the edges of the faces.

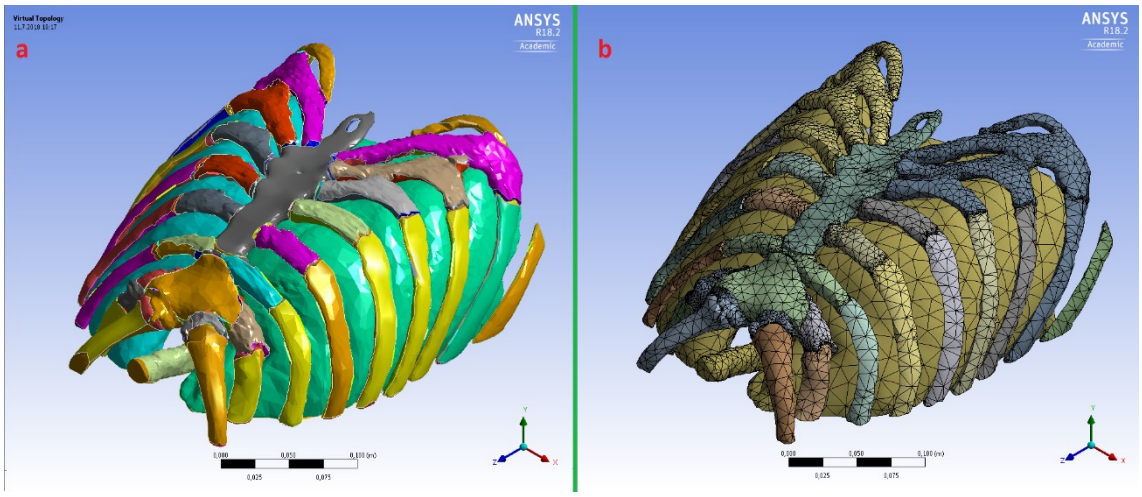

Figure 25. (a) Virtual topology. (b) Finite element mesh created from the virtual topology.

As a result, much cleaner and consistent mesh was obtained but the soft tissue part of the model failed to mesh entirely. The Virtual Topology model of bones, cartilage and lungs worked in the Harmonic Response analysis, but the results were not useful due to lack of rest of the soft tissues.

4.2.4 Cadaver simulation results

Unfortunately, the finite element model built from the cadaver CT-image data ended up not working with any other simulation types but static loads (Figure 26). The importing process resulted in geometry quality which caused mesh related errors when Harmonic Response analysis was used with the mesh. Due to the geometry being imported as faceted solid there was not enough mesh control for solving these issues in meshing phase of ANSYS. Different approached like Virtual Topology and reverse engineering tools in ANSYS SpaceClaim were attempted and Virtual Topology produced working finite element model of bones, cartilage and lungs but failed to successfully mesh the soft tissues. The problems, attempted and possible solutions are explored in more depth in Discussion chapter of the thesis.

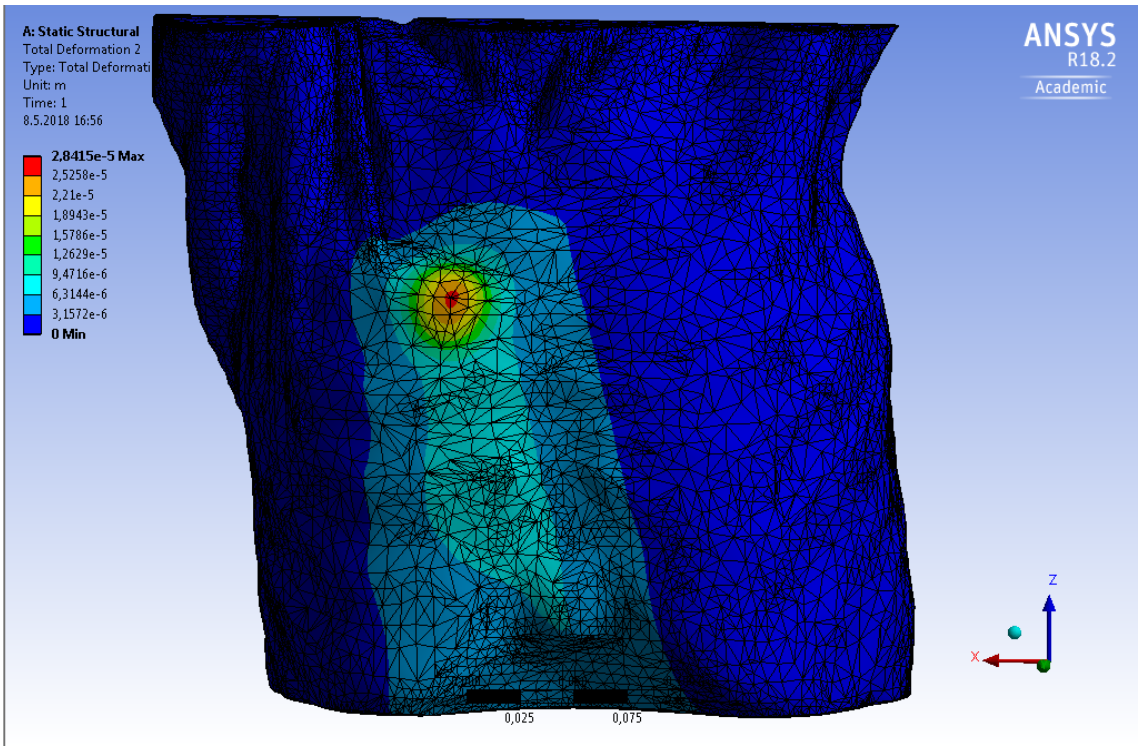

Figure 26. Static load applied on the finite element model of the thorax.

In Figure 26 a static load of 1 N was applied on the third costal cartilage on the right side of the body. The figure shows the how different regions deform as response to the load. It can be noted how the deformation spreads along the sternum. This simulation was only used to test if the finite element mesh worked.

4.3 FEM results from simple thorax models

4.3.1 Simple thorax model 1

In the simulation of the first simple thorax model the effect of where the fixed support was applied to the model was explored and how the material properties for soft tissues would affect the frequency response of the model. In the first simulation case (Figure 27) the fixed support was applied to the end of the “ribs” just like the cadaver model was planned to be used. The Young’s Modulus of the soft tissues was set to 1 MPa like in the literature examples cited before.

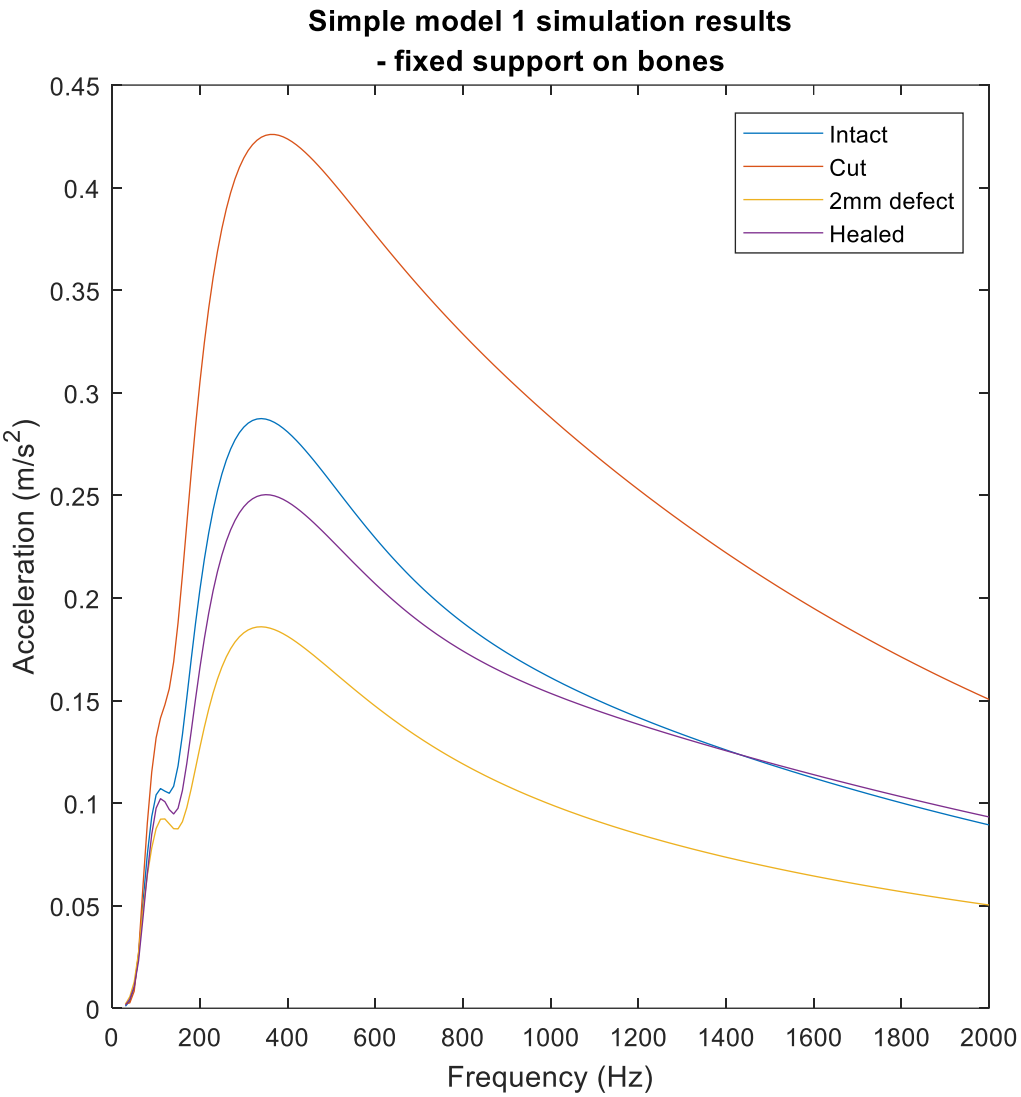

Figure 27. Frequency response of the first simple thorax model.

All contacts were set to "Bonded" with exception of the contact between the halves of the "sternum" in the model where the sternum was cut in half. This contact was set to "Frictionless" as Harmonic Analysis is completely linear and non-linear effects like friction are ignored.

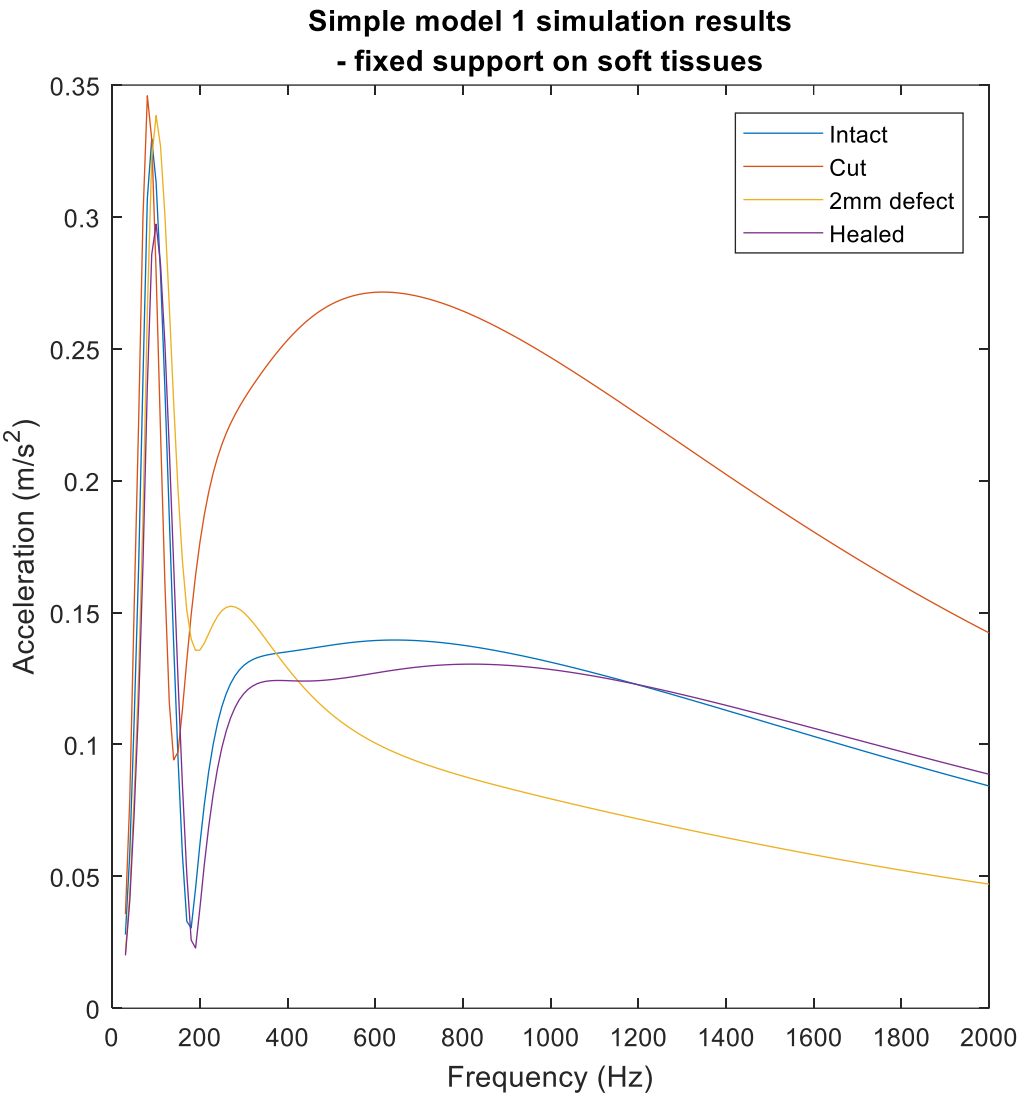

Figure 28. Frequency response of the exactly same model but with fixed support moved to soft tissues.

When the same model was simulated again with fixed support set on the soft tissues the frequency response changed significantly with highest peak present at very low frequencies indicating that the vibration is passing through the soft tissues.

Comparison of the frequency responses in Figure 27 and Figure 28 makes it clear that the location and the tissue type the fixed support is applied to would have large effect on the finite element model of the cadaver. In retrospect it would have been better to segment the entire thorax instead of just the anterior half in order to get more realistic boundary conditions.

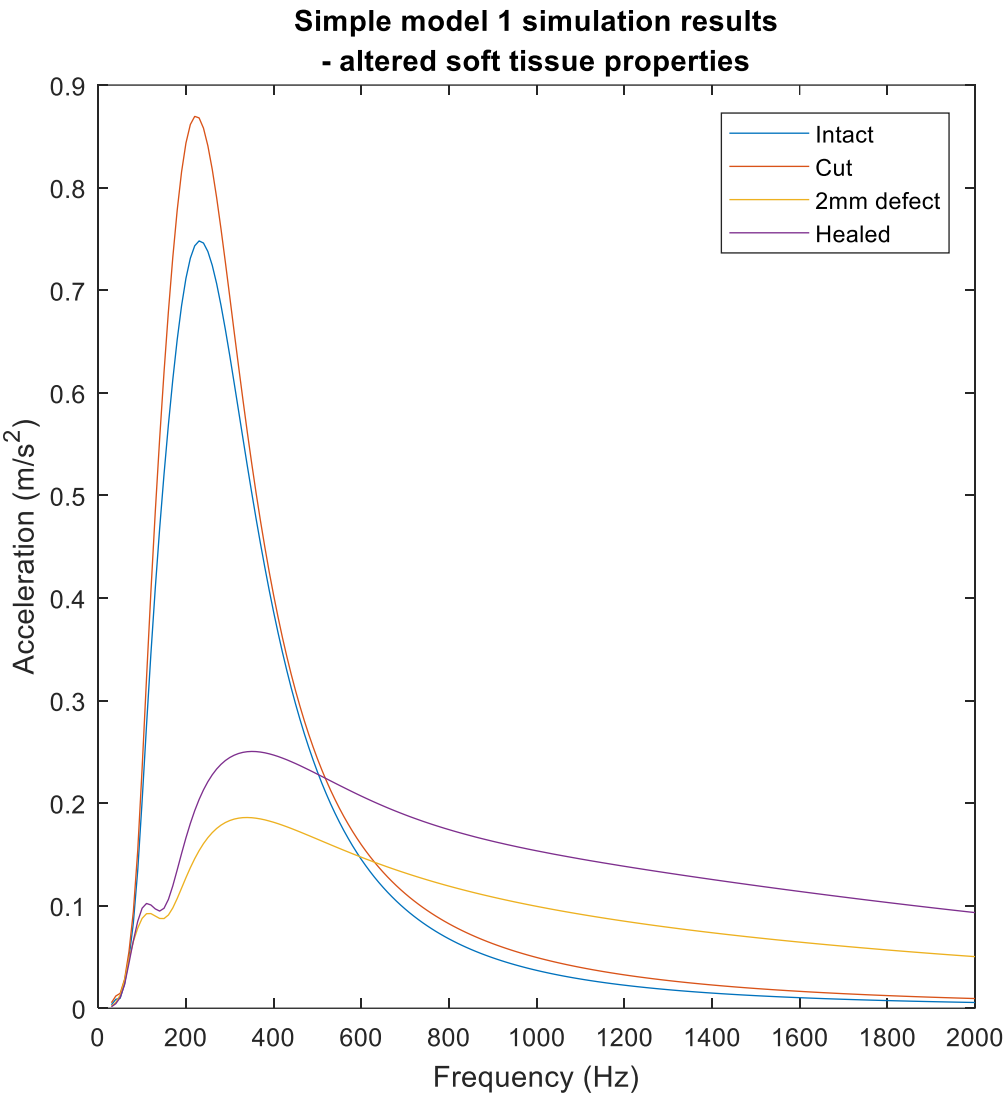

Figure 29. Fixed support was set on bones and Young's Modulus of soft tissues was reduced from 1 MPa to 100 kPa.

Effect of Young's Modulus of the soft tissues was significant and can be seen when comparing Figure 27 and Figure 29. When the stiffness of the soft tissue layer was reduced the vibration was better transmitted through the "sternum" but Figure 29 indicates that the presence of discontinuity in the simulated sternum has larger effect in the simulated model than the material properties of that discontinuity. Even when the 2 mm gap was filled with bone in the simulation of healed sternum it would still not conduct vibration as well as the intact sternum.

4.3.2 Simple thorax model 2

The second simple thorax model was based on CT data from the cadaver. It was used to test effect of material properties and different kind of defects on the vibration transmission through the sternum.

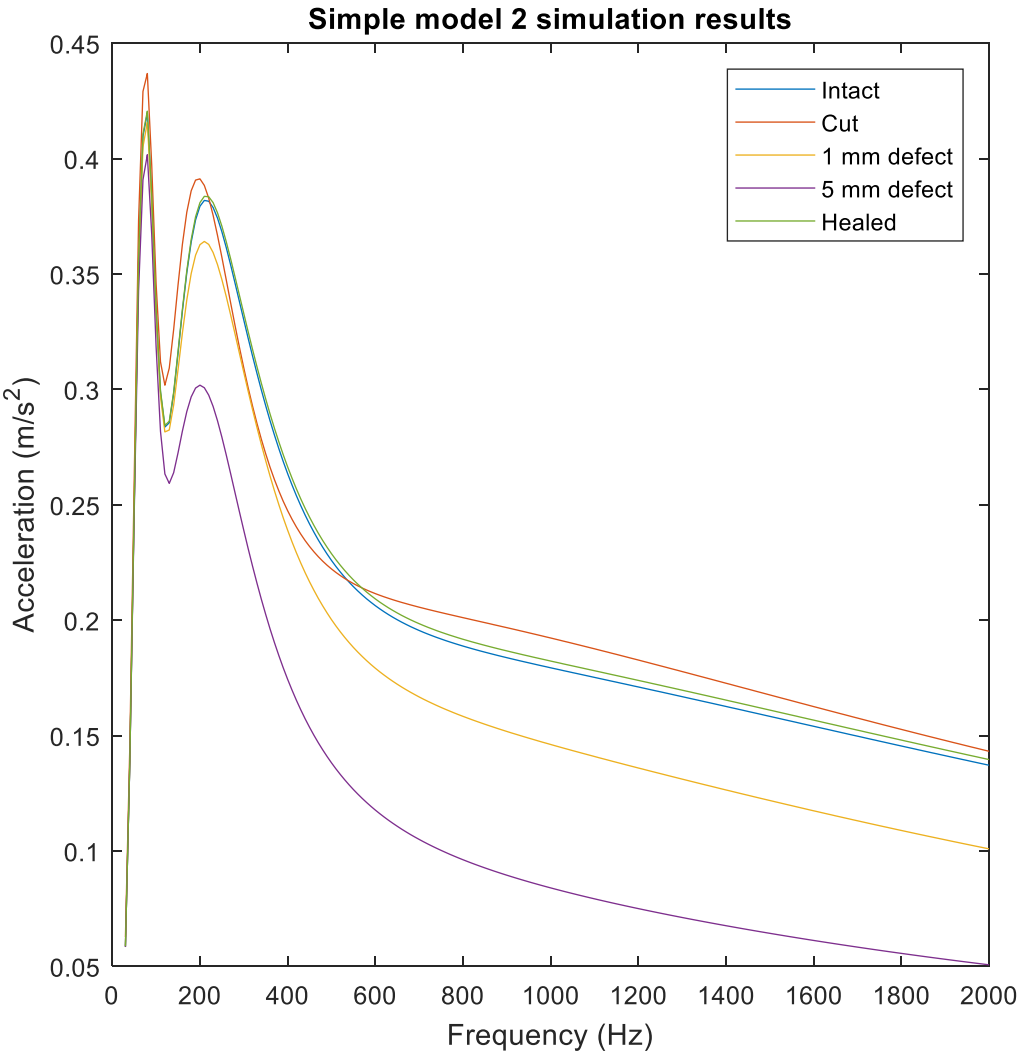

Figure 30. Simulated results from simple thorax model 2 with 1 MPa Young's modulus for the soft tissues. The sternum was simulated in five different conditions.

Simulation results Figure 30 indicate that the defect between the halves of the sternum has to be quite large in order to get significant differences in the frequency response. The first amplitude peak is most likely caused by vibration going through the soft tissues.

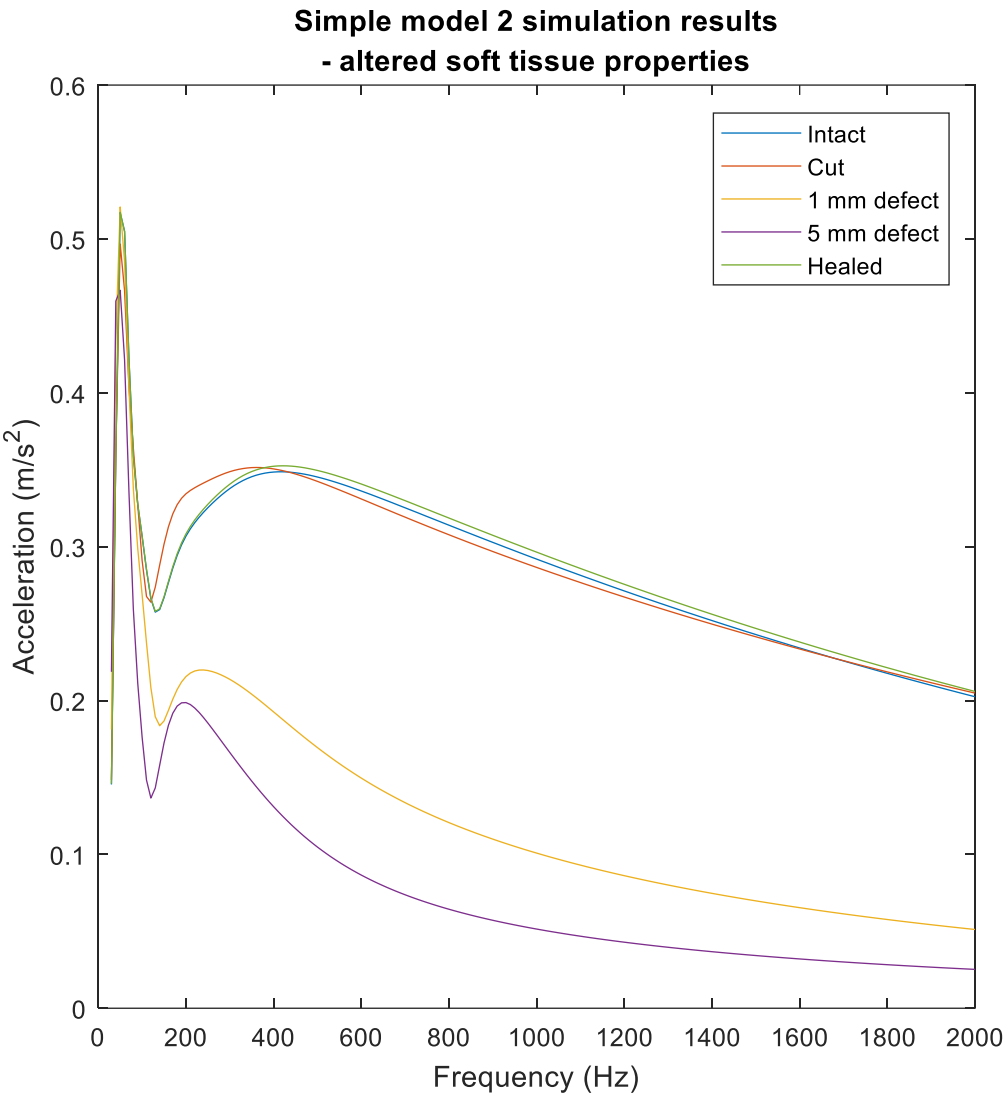

Figure 31. Young's modulus of the soft tissues was reduced to 100 kPa from 1 MPa.

When the Young's modulus of the soft tissues was reduced to 100 kPa (Figure 31) the highest frequency peak occurred at below 100 Hz frequency and difference between sternums with gaps between them and the other sternums grew significantly when compared to the results with stiffer soft tissues (Figure 30).

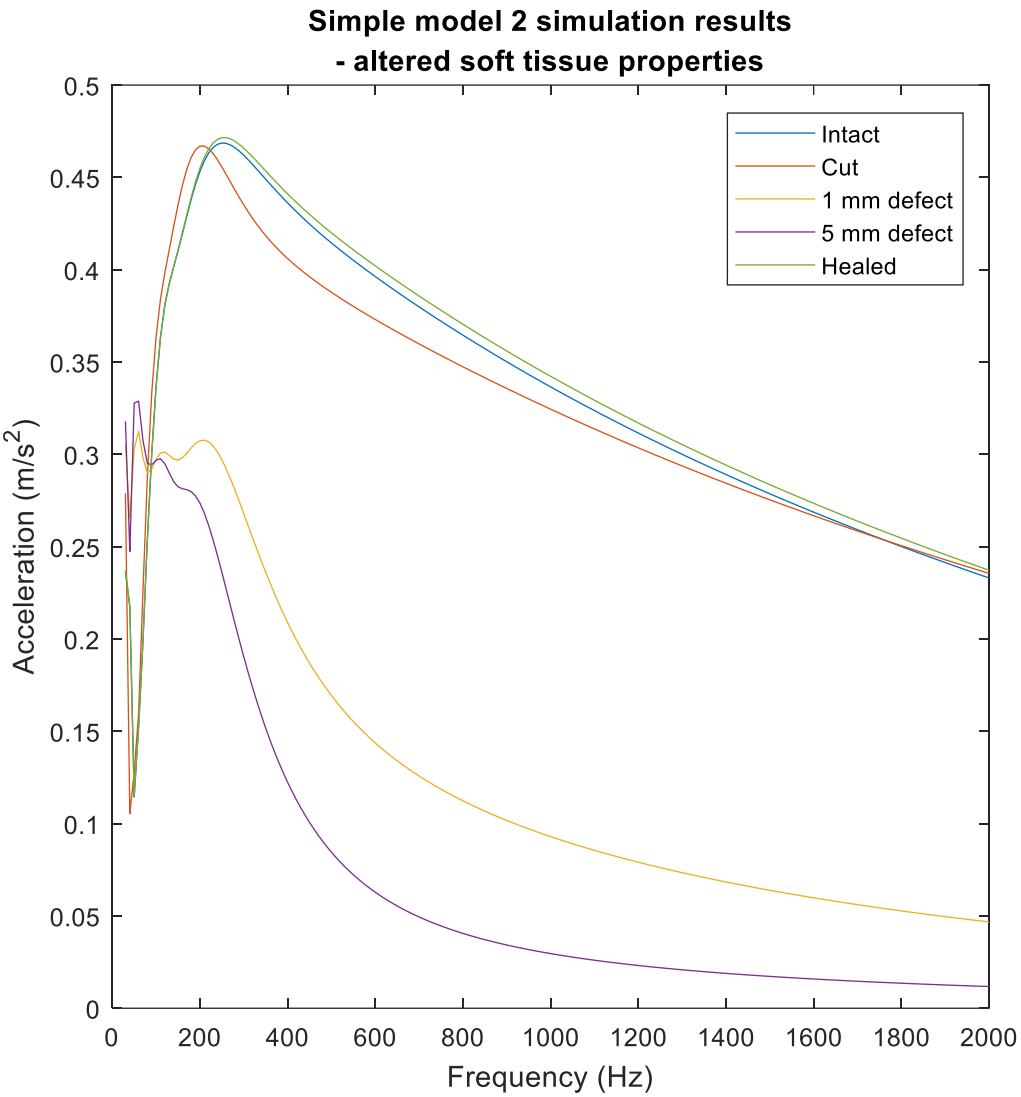

Figure 32. The Young's modulus of the soft tissues was further lowered to 10 kPa to be more in line with material properties of adipose tissue instead of muscle tissue.

When the Young's modulus of the soft tissues was lowered to 10 kPa which is close to that of human adipose tissue [62] the low frequency component is reduced and most of the vibration is conducted through the sternum (Figure 32). This simulation shows again how the simulated sternums with gap between the halves produce different results to the other simulated sternums, but the intact, cut and healed sternums are practically indistinguishable from each other.

5. DISCUSSION

5.1 Reliability of the vibration measurement device

During the phantom measurements it was noticed that both the amplitude and the frequency response of the vibration measurement device are affected by how the operator is holding the actuator. It is possible to press too hard and prevent the actuator from working properly or hold the device too lightly and let the entire actuator module vibrate and move. Both of these actions of the operator had huge impact on the frequency response measured by the accelerometer. The amplitude, power spectral density and at which frequency the amplitude peak is present at are affected.

Unreliability of the data obtained by the vibration measurement device produced a significant problem for the simulation aspect of the thesis. When doing vibration analysis, it is important to have reference data so the model can be matched to its real world counterpart as the simulation includes damping coefficients which have to be manually adjusted for each simulated system and are not obtainable from literature. The lack of reliable real-world data may result in unreliable simulation model.

In addition to the issues with operator's effect on the measurement results there were some technical issues such as the two accelerometer modules bundled with the device producing different results despite using the same accelerometer integrated circuit. Sometimes the device would also write trash data in the result files.

5.2 Importing geometry segmented from CT data to ANSYS

During this thesis it became clear that the tools used (ITK-SNAP, MeshLab, Netfabb, ANSYS SpaceClaim and DesignModeler) were not suitable for creating complex geometry encompassing multiple domains and different tissue types for finite element analysis in ANSYS.

This CAD based approach had been used in other studies to import anatomical structures such as femur to finite element analysis software. In these models the number of different tissue types was low, usually cortical and cancellous bone. For example, when modeling the femur, it is rather easy to create volume for the cancellous bone in the final 3D model by subtracting the volume occupied by the cortical bone and the bone marrow from the total volume of the femur [17]. This volume left over is the volume occupied by the cancellous bone and when using this method there are no gaps in the model.

However, when the same approach was applied in modeling of the thorax problems quickly arose from the interfaces between the costal cartilage, the ribs and the sternum.

The conversion to STL format and smoothing operations would lead to gaps between the bones and the cartilage which would then have to be filled manually by hand or that space would be occupied by soft tissue in the finite element model. This in turn would lead to problems with meshing as thin slivers of soft tissue (muscle, adipose tissue) would be present between the cartilage and the bones and between the lungs and the ribcage and cause the meshing to fail.

Even with significant simplifications to the model, such as reducing the different tissue types from the originally segmented skin, muscle and internal organs, adipose tissue, lungs, cortical bone, cancellous bone and cartilage to just bone, cartilage, lungs and rest of the soft tissues, the mesh quality would be so poor more complex simulations would fail to run. As the importing process produced faceted solids there was little to no control over the mesh inside ANSYS Workbench.

Different approaches such as Virtual Topology in ANSYS Workbench and reverse engineering tools in ANSYS SpaceClaim were attempted to overcome the issue with faceted solids but the complex geometries would either fail to mesh or partially mesh or the reverse engineering tools would fail to create a continuous solid from imported STL file. The Virtual Topology approach provided the most promising results as the cartilage, the bones and the lungs would mesh correctly and run Harmonic Analysis simulation with no issues but meshing of rest of the soft tissues would fail completely.

5.3 Measurement and simulation results from the cadaver, phantoms and simple thorax models

Despite the reliability issues of the vibration measurement device some conclusions can be drawn from the measured data. The data measured from the cadaver clearly shows if the defect is large there is significant difference in the frequency response. However, when tested with the phantoms with much smaller defects the device was unable to differentiate between the embedded PLA rods in intact, cut and sutured conditions. If the defect in the real patient is as significant as the defect created on the cadaver it should be easily palpable and in that case the detection of sternal instability would not require the vibration measurement device. These measurement results indicate that there is some potential in the device, but it would require more development, refinement and testing to determine if vibration measurement can be reliably used to detect smaller defects in the post-sternotomy sternum.

Unfortunately, vibration analysis simulations didn’t work on the cadaver finite element model as described before but the phantoms could be easily simulated as their geometry and material composition was much simpler than the cadavers. This made it easy to bypass the problems with modeling of the cadaver by creating the phantom geometry from scratch and because the number of materials was much lower it was easy to obtain realistic material properties by measurement and from the literature. Number of contact points

between different domains and material types was smaller and the contact types were easier to model realistically.

The simulated phantom results indicate that vibration could be used to detect even smaller defects than those present in the cadaver, but it would require the device to be very accurate and not easily affected by the actions of the operator. In the current iteration of the device the operator can cause larger error in the amplitude response than the simulated difference between intact and cut PLA rods in the phantom.

As the actual cadaver FEM failed to work two simpler models representing sternum and the surrounding tissues were created. The first one was composed of three pairs of ribs, costal cartilage and section of sternum and the surrounding soft tissues limiting to the anterior half of the thorax. When simulating this model, it became apparent that where the boundary conditions, fixed support in this case, were applied had huge effect on the results. This led to the conclusion that modeling just the anterior half of the thorax might not be enough in order to get reliable simulation results.

Another simple thorax model was created based on CT data of the cadaver and different types of sternal defects were simulated on it. Effect of the material properties was also explored. It was noted that the intact, healed and cut sternums were very close to each other while the sternums with gap between the halves produced much lower response to the vibration.

One consistent result from the phantom measurements and simulations and simple thorax model simulations was the shift in frequency response towards the lower end of the spectrum when the vibration has to pass through softer materials such as the ballistic gelatin or soft tissues.

The FEM results should be considered as rough approximates as the systems were modeled as completely linear with no inhomogeneities while their real counterparts have non-linear effects like friction between contact points and non-linear elasticity and anisotropy of materials. Dampening coefficients had significant effect on the FEM results and only in case of the phantom models they could be approximated experimentally by comparing the simulation results to the real measurement results and adjusting the coefficients accordingly. In case of the models attempting to simulate human anatomy, there are other variables like material properties which in humans are depending on many factors like age, exercise and possible pathologies which add further uncertainty to the simulation results.

Despite the shortcomings of the simulation methods used in this thesis he phantom simulation results seemed to most closely match with real world measurement results. They exhibited similar frequency response and similar change in the frequency of the maximum amplitude spike as the real phantoms when the vibration has to pass through softer material.

5.4 Future research

5.4.1 Solutions for geometry and meshing problems

Image based meshing is an alternative for CAD based approach to converting segmented CT data into finite element meshes. In this approach the segmented geometry is never converted into a solid model, but the finite element mesh is created directly from the segmented voxel data or from a STL surface mesh.

According to Young et al. [63] CAD-based meshing approaches become increasingly difficult as the number of domains is increased as the domains have to be converted into surface representations suitable for meshing while preserving the connectivity between them. This was one of the main problems in thesis and Young et al. propose usage of grid-based meshing approach to solve such problems. They mention Simpleware ScanFE as one commercial software which can perform that task and produce high quality finite element meshes from segmented data.

In article by Fang et al. [64] a non-commercial image based meshing tool is presented. The tool is a toolbox for MATLAB and Octave. A surface mesh is extracted from segmented data, possible deficiencies such as isolated vertices and holes in the mesh are repaired and the surface mesh is smoothed. Finally the surface mesh is converted into a 3D tetrahedral volume mesh. However it's unclear if this method is suitable for all types of segmented geometries and if the produced mesh quality is good enough for FEM software like ANSYS.

One possible issue with these approaches is the loss of mesh control in the FEM software used, such as ANSYS and Abaqus. If there is a problem with the mesh, for example sliver elements and elements with poor aspect ratio, the FEM simulation might fail and only solution might be starting the meshing process all over again.

5.4.2 Suggested improvements for the vibration measurement device and measurement procedures

The effect of the how the operator is holding the actuator and the accelerometer module to the measured results should be minimized. The actuator module of the device should be redesigned so that the operator can't have so large effect on the results. The entire actuator module should be in contact with the skin of the subject being measured so the operator would only affect how much the tissue of the measured subject is compressed by the pressure applied instead of compressing the actual actuator against the skin of the subject.

The device could include calibration function for the accelerometer. Easiest way to calibrate an accelerometer is to use the Earth's gravity and simply turn to the accelerometer

180º to get +1 g and -1 g reference points. The calibration procedure could be used to evaluate the health of the accelerometer and avoid problems like garbage data experienced when using current iteration of the device. According to multiple sources calibration of an accelerometer is a prerequisite for accurate measurements [65, 66]. The function of the accelerometer should be also tested with a known vibration source.

Frequency sweeps should be equal in length, currently the device returns measured data files with varying sweep lengths and some of the measurements include a lot of trailing zeroes. This could be caused by some software error or inconsistent vibration sweep length.

In case of the cadaver measurements a smaller defect such as only partial sternal dehiscence or smaller gap than the 5 mm could be more useful in determining if the device can detect beginning of sternal dehiscence before it becomes clearly symptomatic and palpable to hand. The larger defects used in the cadaver measurements could be replicated in the phantoms to determine if they produce similar results.

6. CONCLUSIONS

When this thesis was started the idea was simple; take measurements from a cadaver, segment geometry from CT image of the same cadaver and create a finite element model which will be adjusted to match the measurements from the cadaver and test different kind of defects on the same model to predict how they would affect the frequency response to the vibration sweep. It was assumed that CAD and FEM tools had evolved far enough to make the conversion process simple and that modeling vibration in modern FEM software like ANSYS would be rather easy. These assumptions were based on previous research performed on simpler geometry and static loads. Unfortunately, both of these assumptions turned out to be wrong.

The segmentation itself was successful. It was performed with ITK-SNAP 3.6.0. The geometry exported from ITK-SNAP was edited with MeshLab v2016.12 and Autodesk Netfabb Standard 2017 to smooth out the coarse surfaces and to reduce the number of polygons. The conversion to solid format was performed with ANSYS SpaceClaim 18.2 and meshing and simulation tests were completed in ANSYS 18.2. Models for the phantoms and the simple thoraxes were created with ANSYS SpaceClaim 18.2. MATLAB was used to analyze and plot the results from both measurements and simulations.

After working over 6 months on the complex thorax models it was realized that the CAD based approach chosen for the thesis would not work. Further solutions such as using Virtual Topology were attempted to no avail. At this point the conclusion was that the problem was approached from too complex direction with too many variables and a simpler approach was required. So, the phantoms were built, measured and modeled. At this point the uncertainties of the results produced by the vibration measurement device and the difficulty of modeling vibration in ANSYS were discovered.

In the end most usable results were obtained from the measured and simulated phantoms and that experience was used to build to simpler geometries representing a sternum and the surrounding tissues. Different kind of defects were successfully simulated on these simple models. The results indicate that detecting major defects with vibration is easy but smaller defects may remain unnoticed. One consistently appearing result was the shift in frequency response towards lower end of the spectrum when the vibration had to pass through softer materials.

A lot of work and research went into exploring the function of the vibration measurement device with means of measurements and simulation. While the results are far from conclusive they indicate there is potential in the device but also reveal some improvements in the design are required for increased accuracy and repeatability of the measurement results.

REFERENCES

[1] B. Bordoni, F. Marelli, B. Morabito, B. Sacconi, P. Severino, Post-sternotomy pain syndrome following cardiac surgery: case report, Journal of pain research, Vol. 10, 2017, pp. 1163. Available (accessed pmid:28553137).

[2] D.A. Ott, D.A. Cooley, R.T. Solis, C.B. Harrison, Wound complications after median sternotomy: A study of 61 patients from a consecutive series of 9,279, Cardiovascular Diseases, Vol. 7, Iss. 1, 1980, pp. 104-111. Available (accessed J1: Cardiovasc Dis): http://www.ncbi.nlm.nih.gov/pmc/articles/PMC287839/.

[3] V.A. Olbrecht, C.J. Barreiro, P.N. Bonde, J.A. Williams, W.A. Baumgartner, V.L. Gott, J.V. Conte, Clinical outcomes of noninfectious sternal dehiscence after median sternotomy, The Annals of Thoracic Surgery, Vol. 82, Iss. 3, 2006, pp. 902-907.

[4] Postoperative Sternal Stability Assessed by Vibration: A Preliminary Study, in: The Annals of Thoracic Surgery, 2012, pp. 260-264.

[5] C.Y. Bitkover, K. Cederlund, B. Åberg, J. Vaage, Computed tomography of the sternum and mediastinum after median sternotomy, The Annals of Thoracic Surgery, Vol. 68, Iss. 3, 1999, pp. 858-863. Available (accessed doi: 10.1016/S0003-4975(99)00549-4; 28): http://dx.doi.org/10.1016/S0003-4975(99)00549-4.

[6] Assessment of sternal instability by vibration: Master of Science Thesis, Tamperere University of Technology, Tampere, 2010, .

[7] D.L. Logan, A first course in the finite element method, Cengage Learning, 2011, .

[8] A.L. Didier, P.F. Villard, J. Saad, J.M. Moreau, M. Beuve, B. Shariat, A chest wall model based on rib kinematics, Proceedings - 2009 2nd International Conference in Visualisation, VIZ 2009, pp. 159-164.

[9] Fundamental study of side impact analysis using the finite element model of the human thorax, in: JSAE Review, 2001, pp. 195-199.

[10] J. Awrejcewicz, B. Łuczak, The finite element model of the human rib cage, Journal of Theoretical and Applied Mechanics, Vol. 45, Iss. 1, 2007, pp. 25-32.

[11] B. Gzik-Zroska, W. Wolański, M. Gzik, Engineering-aided treatment of chest deformities to improve the process of breathing, International journal for numerical methods in biomedical engineering, Vol. 29, Iss. 9, 2013, pp. 926-937.

[12] M.L. Oyen, D. Murakami, R.W. Kent, Mechanical Characterization of Costal Cartilage, 33rd Proceedings of the International Workshop on Human Subjects for Biomechanical Research.

[13] G.Z. Zhang, X. Chen, J. Ohgi, T. Miura, A. Nakamoto, C. Matsumura, S. Sugiura, T. Hisada, Biomechanical simulation of thorax deformation using finite element approach, BIOMEDICAL ENGINEERING ONLINE, Vol. 15, Iss. 1, 2016, pp. 18.

[14] M. Iwamoto, Y. Kisanuki, I. Watanabe, K. Furusu, K. Miki, J. Hasegawa, Development of a finite element model of the total human model for safety (THUMS) and application to injury reconstruction, Proceedings of the 2002 International Research Council on Biomechanics of Injury, Munich, Germany, 2002, pp. 31-42.

[15] E. Song, X. Trosseille, P. Baudrit, Evaluation of thoracic deflection as an injury criterion for side impact using a finite elements thorax model, Stapp car crash journal, Vol. 53, 2009, pp. 155-191.

[16] B. Couteau, M. Hobatho, R. Darmana, J. Brignola, J. Arlaud, Finite element modelling of the vibrational behaviour of the human femur using CT-based individualized geometrical and material properties, Journal of Biomechanics, Vol. 31, Iss. 4, 1998, pp. 383-386.

[17] S. Abe, Influence of Exercise History on the Proximal Femur Strength; Finite Element Analysis of Female Athletes, 2013, Available: http://tut.summon.serialssolutions.com/2.0.0/link/0/eLvHCXMwjV1NS8NAEB1svYgeFBWtCnP0ko_uJk2Cp1ITakXw4EG9hE121xZsAiEB_ffObqyKp96HYWZgZ2aZeW8AOHN9519O8H3JhZJaa8kjrv1CizIupSrEpOCssFjlV_bwHC4W8csvrFvSqzJ3Nkq37VqXgi3JSK_nH_Ao51L1j-LEY4bxZAADHgVD2J1N79M5lYp2A9yzpSI7hP3bPyPuI9hR1TEs7za3QLDWmH6fOcKeo-MT6wqpD8PHpv5YrcU7Zmrd-NWgGxtVbu7zBbGU6Q0z7VW_cElkYXSRKKR6nZieCusYT8LL0aTZ3yKy89ys31M62ZBlAR_7jT2794adwIMyWe9VaNJw8A0woTQahjMpwXATU64hJE-heBZvQVVCrk-hyut1U_2l70AvZYfwTCGbNLGLZNp65sfL8AyciSwQ.

[18] K.S. Saladin, Human Anatomy, McGraw-Hill Higher Education, 2004.

[19] F.H. Netter, Atlas of Human Anatomy, Elsevier Health Sciences, 2010.

[20] B. Atkins Zane, G. Wolfe Walter, Sternal Wound Complications Following Cardiac Surgery, in: Narin Cuneyt (ed.), Special Topics in Cardiac Surgery, InTech, https://www.intechopen.com/books/special-topics-in-cardiac-surgery/sternal-wound-complications-following-cardiac-surgery, 2012.

[21] L. Kaiser, I.L. Kron, T.L. Spray, Spray, Division of Cardiothoracic Surgery Thomas L, Mastery of Cardiothoracic Surgery, 3th ed. LWW, Philadelphia, 2013.

[22] H. Kubota, H. Miyata, N. Motomura, M. Ono, S. Takamoto, K. Harii, N. Oura, S. Hirabayashi, S. Kyo, Deep sternal wound infection after cardiac surgery, Journal of Cardiothoracic Surgery, Vol. 8, Iss. 1, 2013, pp. 132. Available (accessed ID: Kubota2013): https://doi.org/10.1186/1749-8090-8-132.

[23] K. Aykut, G. Albayrak, A. Kavala, M. Guzeloglu, K. Karaarslan, E. Hazan, Early Repair of Sternal Instability Prevents Mediastinitis, World Journal of Cardiovascular Surgery, Vol. 4, Iss. 2, 2014, pp. 13-16.

[24] T.J. Francel, A rational approach to sternal wound complications, Seminars in thoracic and cardiovascular surgery, Vol. 16, Iss. 1, 2004, pp. 81-91. Available (accessed LR: 20161124; JID: 8917640; 2004/09/16 05:00 [pubmed]; 2004/11/09 09:00 [medline]; 2004/09/16 05:00 [entrez]; ppublish).

[25] P.M. Boiselle, A.V. Mansilla, M.S. Fisher, T.C. McLoud, Wandering wires: frequency of sternal wire abnormalities in patients with sternal dehiscence, American Journal of Roentgenology, Vol. 173, Iss. 3, 1999, pp. 777-780. Available (accessed doi: 10.2214/ajr.173.3.10470922; 01): https://doi.org/10.2214/ajr.173.3.10470922.

[26] D. El-Ansary, R. Adams, L. Toms, M. Elkins, Sternal instability following coronary artery bypass grafting, 2009, 27-33 p.

[27] P.M. Boiselle, A.V. Mansilla, C.S. White, M.S. Fisher, Sternal dehiscence in patients with and without mediastinitis, Journal of thoracic imaging, Vol. 16, Iss. 2, 2001, pp. 106-110. Available (accessed LR: 20161124; JID: 8606160; 2001/04/09 10:00 [pubmed]; 2001/08/10 10:01 [medline]; 2001/04/09 10:00 [entrez]; ppublish): .

[28] A.E. Li, E.K. Fishman, Evaluation of Complications After Sternotomy Using Single- and Multidetector CT with Three-Dimensional Volume Rendering, American Journal of Roentgenology, Vol. 181, Iss. 4, 2003, pp. 1065-1070. Available (accessed doi: 10.2214/ajr.181.4.1811065; 28): https://doi.org/10.2214/ajr.181.4.1811065.

[29] D. El-Ansary, G. Waddington, R. Adams, Measurement of non-physiological movement in sternal instability by ultrasound, The Annals of Thoracic Surgery, Vol. 83, Iss. 4, 2007, pp. 1513-1516. Available (accessed LR: 20161124; JID: 15030100R; CIN: Ann Thorac Surg. 2007 Apr;83(4):1516-7. PMID: 17383369; 2006/05/29 00:00 [received]; 2006/10/17 00:00 [revised]; 2006/10/23 00:00 [accepted]; 2007/03/27 09:00 [pubmed]; 2007/04/14 09:00 [medline]; 2007/03/27 09:00 [entrez]; ppublish): .

[30] L.H. Sperling, Sound and vibration damping with polymers: Basic viscoelastic definitions and concepts, in: Anonymous (ed.), ACS Publications, 1990, .

[31] D.A. Harris, Noise control manual, Van Nostrand Reinhold, Vol. 3, 1991, pp. 45-53.

[32] C.W. De Silva, Vibration damping, control, and design, CRC Press, 2007, .

[33] J.M. Wakeling, B.M. Nigg, A.I. Rozitis, Muscle activity damps the soft tissue resonance that occurs in response to pulsed and continuous vibrations, Journal of applied physiology, Vol. 93, Iss. 3, 2002, pp. 1093-1103.

[34] A. Tsuchikane, Y. Nakatsuchi, A. Nomura, The influence of joints and soft tissue on the natural frequency of the human tibia using the impulse response method, Proceedings of the Institution of Mechanical Engineers, Part H: Journal of Engineering in Medicine, Vol. 209, Iss. 3, 1995, pp. 149-155.

[35] In vivo assessment of bone mechanical properties by vibration and ultrasonic wave propagation analysis, in: Bone, 1996, pp. S35.

[36] S.G. Roberts, C.R. Steele, Efficacy of monitoring long-bone fracture healing by measurement of either bone stiffness or resonant frequency: Numerical simulation, Journal of Orthopaedic Research, Vol. 18, Iss. 5, 2000, pp. 691-697.

[37] A. Rowlands, F.A. Duck, J.L. Cunningham, Bone vibration measurement using ultrasound: Application to detection of hip prosthesis loosening, Medical Engineering and Physics, Vol. 30, Iss. 3, 2008, pp. 278-284. Available (accessed pmid:17587635).

[38] L. Nokes, J.A. Fairclough, W.J. Mintowt-Czyz, I. Mackie, J. Williams, Vibration analysis of human tibia: the effect of soft tissue on the output from skin-mounted accelerometers, Journal of Biomedical Engineering, Vol. 6, Iss. 3, 1984, pp. 223-226.

[39] G. Dhatt, G. Touzot, E. Lefrançois, Introduction, Finite Element Method, John Wiley & Sons, Inc., 2012, pp. 1-19.

[40] S. Moaveni, Finite Element Analysis Theory and Application with ANSYS, 3rd ed. Prentice-Hall, Inc, Upper Saddle River, NJ, USA, 2007.

[41] J.N. Reddy, An introduction to the finite element method, 3rd ed. McGraw-Hill Higher Education, New York, NY, 2006.

[42] K.J. Bathe, Finite Element Procedures, Prentice Hall, 2006.

[43] T. Ota, I. Yamamoto, R. Morita, Fracture simulation of the femoral bone using the finite-element method: How a fracture initiates and proceeds, Journal of bone and mineral metabolism, Vol. 17, Iss. 2, 1999, pp. 108-112. Available (accessed ID: Ota1999): https://doi.org/10.1007/s007740050072.

[44] Z. Yosibash, N. Trabelsi, C. Milgrom, Reliable simulations of the human proximal femur by high-order finite element analysis validated by experimental observations, Journal of Biomechanics, Vol. 40, Iss. 16, 2007, pp. 3688-3699. Available (accessed pmid:17706228).

[45] O.L.A. Harrysson, Y.A. Hosni, J.F. Nayfeh, Custom-designed orthopedic implants evaluated using finite element analysis of patient-specific computed tomography data: femoral-component case study, BMC Musculoskeletal Disorders, Vol. 8, Iss. 1, 2007, pp. 91. Available (accessed ID: Harrysson2007): https://doi.org/10.1186/1471-2474-8-91.

[46] C.A. Taylor, T.J.R. Hughes, C.K. Zarins, Finite Element Modeling of Three-Dimensional Pulsatile Flow in the Abdominal Aorta: Relevance to Atherosclerosis, Annals of Biomedical Engineering, Vol. 26, Iss. 6, 1998, pp. 975-987. Available (accessed ID: Taylor1998): https://doi.org/10.1114/1.140.

[47] A.K. Venkatasubramaniam, M.J. Fagan, T. Mehta, K.J. Mylankal, B. Ray, G. Kuhan, I.C. Chetter, P.T. McCollum, A Comparative Study of Aortic Wall Stress Using Finite Element Analysis for Ruptured and Non-ruptured Abdominal Aortic Aneurysms, European Journal of Vascular and Endovascular Surgery, Vol. 28, Iss. 2, 2004, pp. 168-176. Available (accessed doi: 10.1016/j.ejvs.2004.03.029; 15): http://dx.doi.org/10.1016/j.ejvs.2004.03.029.

[48] T.C. Gasser, M. Auer, F. Labruto, J. Swedenborg, J. Roy, Biomechanical Rupture Risk Assessment of Abdominal Aortic Aneurysms: Model Complexity versus Pre-

dictability of Finite Element Simulations, European Journal of Vascular and Endovascular Surgery, Vol. 40, Iss. 2, 2010, pp. 176-185. Available (accessed doi: 10.1016/j.ejvs.2010.04.003; 15): http://dx.doi.org/10.1016/j.ejvs.2010.04.003.

[49] E.M. Alawadhi, Finite element simulations using ANSYS, CRC Press, 2015.

[50] M. Virta, The capabilities of the fused deposition modeling machine Ultimaker and its adjusting for the biomedical research purposes, 2014, Available: http://tut.summon.serialssolutions.com/2.0.0/link/0/eLvHCXMwjV1NT8MwDLXYuCA4gADxKfnIZW1J2zU9orFpGuIG4uNSpUkqBmxDa3rh12OnDBCn3aPIdpQ8R_bzA4hFEPXvQkZzzFPdWZ0Xl3G0iZlJJUyul_KSBkvIfnwLG4f08lEPv3Sug3dKtbZ0IFrXEDBNmRk2M4fCOnNJfTPZB4KFqXuQCfOki5sDq5uhmOCCrci7nmoGO3C9vWfEvcebNj5PnzSaaAmXPKtqPQ5xUW-FlHph1dTWoLGr3in0yjQEJzjzXY4W79_ddKbe7BLJHpy6GpV5ZQkuWkMJp9-l5dBzuPF7eM8LflAEF7WtDyAcDe8G4x4ZWrSeFjzs2YMYUzyKHw8L72F8CDuK-97nzvPjzBFgpESVmqTkAib_dBnedZUKHVeZzWV-DBfrbn-y_tJT2KLEIeE-quuifQdctG3vuI_4F3zGYuQ.

[51] J. Torres, J. Cotelo, J. Karl, A.P. Gordon, Mechanical property optimization of FDM PLA in shear with multiple objectives, JOM, Vol. 67, Iss. 5, 2015, pp. 1183-1193.

[52] Janne T Koivisto, Tiina Joki, Jenny E Parraga, Rami Pääkkönen, Laura Ylä-Outinen, Laura Salonen, Ilari Jönkkäri, Marja Peltola, Teemu O Ihalainen and Susanna Narkilahti Bioamine-crosslinked gellan gum hydrogel for neural tissue engineering, in: Biomedical Materials, IOP Publishing, 2017, pp. 025014.

[53] R.K.A. Pasumarthy, H.V. Tippur, Mechanical and optical characterization of a tissue surrogate polymer gel, Polymer Testing, Vol. 55, 2016, pp. 219-229.

[54] Clear Ballistics - 10% Ballistic Gelatin FBI Block, https://www.clearballistics.com/shop/10-ballistic-gelatin-fbi-block/.

[55] N. Ribeiro, P.C. Fernandes, D. Lopes, J. Folgado, P. Fernandes, 3-D Solid and Finite Element Modeling of Biomechanical Structures—A Software Pipeline, pp. 2-17.

[56] G. Taubin, Curve and surface smoothing without shrinkage, IEEE, pp. 852-857.

[57] W. Murphy, J. Black, G.W. Hastings, Handbook of biomaterial properties, Springer, 2016.

[58] J.Y. Rho, R.B. Ashman, C.H. Turner, Young's modulus of trabecular and cortical bone material: ultrasonic and microtensile measurements, Journal of Biomechanics, Vol. 26, Iss. 2, 1993, pp. 111-119. Available (accessed pmid:8429054).

[59] F. Liu, D.J. Tschumperlin, Micro-mechanical characterization of lung tissue using atomic force microscopy, Journal of visualized experiments: JoVE, Iss. 54, 2011, Available (accessed pmid:21897356).

[60] R.G. Wells, Tissue mechanics and fibrosis, Biochimica et Biophysica Acta (BBA)-Molecular Basis of Disease, Vol. 1832, Iss. 7, 2013, pp. 884-890.

[61] C.G. Rhodes, P. Wollmer, F. Fazio, T. Jones, Quantitative measurement of regional extravascular lung density using positron emission and transmission tomography. Journal of computer assisted tomography, Vol. 5, Iss. 6, 1981, pp. 783-791. Available (accessed pmid:6976359).

[62] N. Alkhouli, J. Mansfield, E. Green, J. Bell, B. Knight, N. Liversedge, J.C. Tham, R. Welbourn, A.C. Shore, K. Kos, The mechanical properties of human adipose tissues and their relationships to the structure and composition of the extracellular matrix, American Journal of Physiology-Endocrinology and Metabolism, Vol. 305, Iss. 12, 2013, pp. E1435.

[63] P.G. Young, T. Beresford-West, S. Coward, B. Notarberardino, B. Walker, A. Abdul-Aziz, An efficient approach to converting three-dimensional image data into highly accurate computational models, Philosophical Transactions of the Royal Society of London A: Mathematical, Physical and Engineering Sciences, Vol. 366, Iss. 1878, 2008, pp. 3155-3173. Available (accessed pmid:18573757).

[64] Q. Fang, D.A. Boas, Tetrahedral mesh generation from volumetric binary and grayscale images, Ieee, pp. 1142-1145.

[65] The Basics of Accelerometer Calibration , http://modalshop.com/filelibrary/Basics%20of%20Calibration.pdf.

[66] C. Vogler, Calibration of Accelerometer Vibration Sensitivity by Reference, 2015.